4

Seismic Signals and Noise

Peter Bormann

4.1 Nature and presentation of seismic signals and noise

As shown in Fig. 1.1, one of the key problems in seismology is to solve the inverse problem, i.e., to derive from the analysis of seismic records information about the structure and physical properties of the Earth medium through which the seismic waves propagate (see Chapter 2) as well as about the geometry, kinematics and dynamics of the seismic source process (see Chapter 3). This task is complicated by the fact that the seismic signals radiated by the source are weakened and distorted by geometric spreading and attenuation and, due to reflection, diffraction, mode conversion and interference during their travel through the Earth. They are also distorted by the *transfer function* of the seismograph. While the Earth acts as a low-pass filter by attenuating higher frequencies most effectively, a mechanical seismograph is a second order high-pass filter with a roll-off of –12 dB per octave for periods larger than its eigenperiod (see Chapter 5).

Additionally, seismic signals are superposed and, in the case of low *signal-to-noise ratio* (SNR), sometimes completely masked by seismic noise. Therefore, one of the main issues in applied seismology is to ensure high SNR or, where conditions are bad, to improve it by suitable ways of data acquisition and processing. The success of SNR improvement largely depends on our understanding of the ways in which seismic signals and noise differ.

4.1.1 Seismic signals

The signal radiated from a seismic source, be it an explosion or a shear rupture, is usually a more or less complicated displacement step function or velocity impulse of finite duration from milliseconds up to a few minutes at the most (see Figs. 2.4, 3.4 and 3.7). According to the *Fourier theorem* any arbitrary *transient function* f(t) in the *time domain* can be represented by an equivalent function F(ω) in the *frequency domain*, the *Fourier transform* of f(t). The following relations hold:
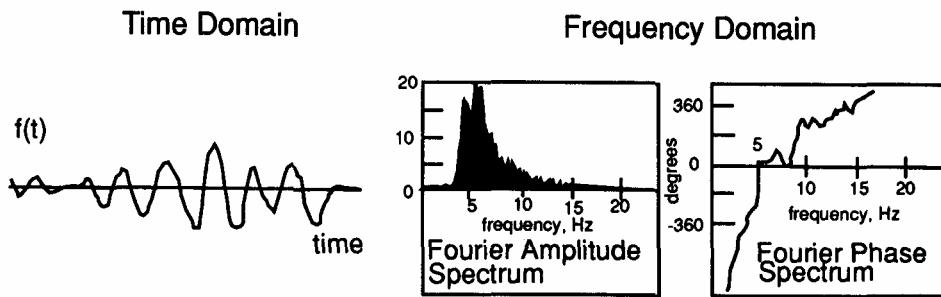
$$f(t) = (2\pi)^{-1} \int_{-\infty}^{\infty} F(\omega) \exp(i\omega t)\, d\omega \tag{4.1}$$

$$F(\omega) = \int_{-\infty}^{\infty} f(t) \exp(-i\omega t)\, dt = |F(\omega)| \exp(i\phi(\omega)) \quad . \tag{4.2}$$
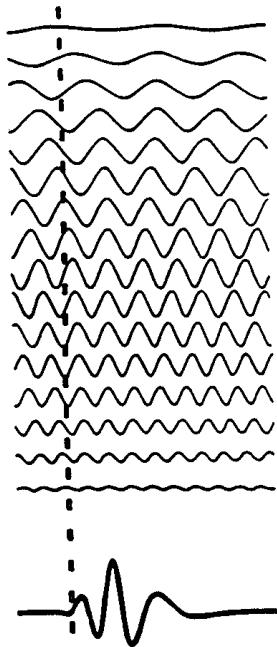
(Note that other sign conventions are often used, e.g. exp(-$i\omega$ t) in Eq. (4.1) and exp($i\omega$ t) in Eq. (4.2) in wave propagation studies in order to assure that the wave-number vector is positive in the direction of wave propagation).
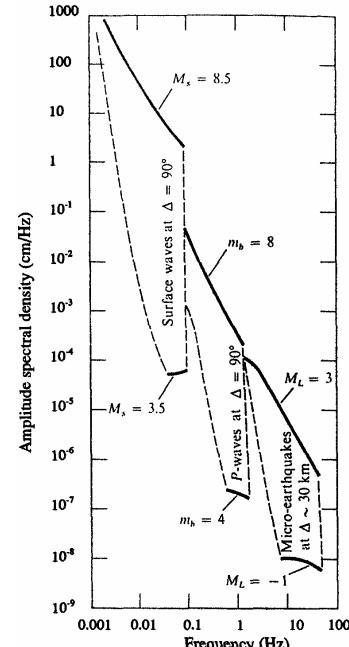
$\left|F(\omega)\right| = A(\omega)$ is the *amplitude spectral density* with the unit m/Hz, $\omega = 2\pi f$ the angular frequency (with f - frequency in unit Hz) and $\phi(\omega)$ the *phase spectrum* with the units deg, rad or 2πrad. Fig. 4.1 gives an example. The integral in (4.1) is equivalent to a sum. Thus, the *Fourier theorem* states that an arbitrary finite time series, even an impulsive one, can be expressed as a sum of monochromatic periodic functions, i.e., $f(t) = 2\pi^{-1} \sum \left|F(\omega)\right| \exp(i[\omega t + \phi(\omega)])\Delta\omega$. Fig. 4.2 illustrates how a sum of harmonic terms can equal an arbitrary function.


Fig. 4.1 A signal recorded as a function of time (left) can be represented equivalently in the frequency domain by its Fourier spectrum. The amplitude (middle) and phase spectrum (right) are both needed to provide the complete time series (reproduced from Lay and Wallace, 1995, Figure 5.B1.1, p. 176; with permission of Elsevier Science (USA)).


Fig. 4.2 The transient signal f(t) is formed by summing up the infinite harmonic terms of a discretized version of Eq. (4.1). The amplitudes of each harmonic term vary, being prescribed by the amplitude spectrum. The shift of the phase of each harmonic term is given by the phase spectrum (reproduced from Lay and Wallace, 1995, Figure 5.B1.2, p. 177; with permission of Elsevier Science (USA)).
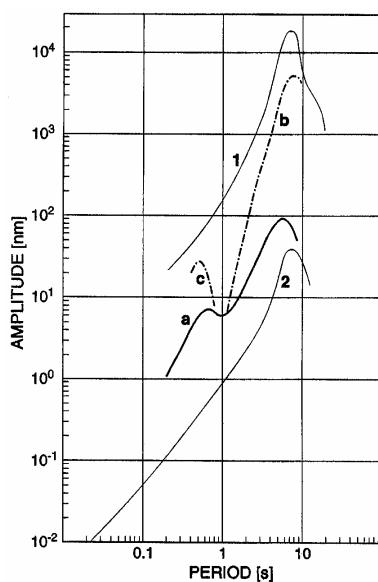
Fig. 4.3 Ranges of amplitude spectral densities for seismic waves. The lower bound is limited due to ambient seismic noise (according to Aki and Richards, 1980; with kind permission of the authors).

By high-, low- or band-pass filtering of an input signal, such as the one shown in Fig. 4.2, the amplitudes and phase relationships of its harmonic terms and thus the shape, amplitude and pre-dominant period of the resulting output signal are changed. Examples will be given in 4.2.1 below. Therefore, magnitudes of seismic events determined from amplitude and period readings of seismic phases are comparable only when determined from analog seismic records with identical standard frequency responses or digital records filtered appropriately. Systematic differences between various magnitude scales as well as saturation effects are the consequence of filtering the input signals with different responses and in limited frequency ranges (see 3.2.7 and Fig. 3.18). Fig. 4.3 presents the range of amplitude spectral densities for seismic waves above the level of ambient seismic noise, depending on magnitude and distance.

4.1.2 Seismic noise

While the harmonic components of transient seismic signals radiated by localized sources of finite duration are coherent and their phase relationships defined by the phase spectrum, this is not the case for ambient seismic noise. The latter is caused by a diversity of different, spatially distributed, mostly unrelated and often continuous sources (see 4.3). Seismic noise (for records see 4.3) thus forms a more or less *stationary stochastic process* without a defined phase spectrum. The same applies to electronic instrumental self-noise and the Brownian (thermal) motion of the seismic mass (see 5.6). Early efforts in the years of analog seismology to get a quantitative measure of seismic noise as a function of frequency were based on drawing envelopes of peak amplitude readings in given time intervals for seismic noise at different times of the day and year. Such presentations are not commensurate when based on records or filtered time plots of different bandwidth and can not resolve spectral details (Fig. 4.4).


Fig. 4.4 Envelopes of maximum and minimum peak amplitudes for rural environments as determined from analog seismograph records of different type over a long time-span according to Brune and Oliver (1959) (curves 1 and 2: high- and very low-noise sites, respectively; bandwidth of recordings 1 to 2 octaves) together with envelope curves of peak noise amplitudes at station MOX, Germany, at times of minimum (a) and maximum noise (b and c; bandwidth of records 4 to 8 octaves) (reproduced from Journal of Seismology, 2, 1998, "Conversion and…", P. Bormann, p. 38, Fig. 1; © Kluwer Academic Publishers, with permission of Kluwer Academic Publishers).

4. Seismic Signals and Noise

Instructions for reporting microseisms with periods > 2s to be measured regularly at 00h, 06h, 12h and 18h daily, were given in the 1979 edition of MSOP (Willmore, 1979), Chapter on Reporting output. This is no longer practised in times of digital seismology and the possibility for computational spectral analysis. However, because of the stochastic nature of seismic noise, the integral in Eq. (4.2) does not converge. Consequently, *amplitude spectral density* and *phase spectrum* can not be calculated. Instead, we have to determine the *power spectral density* $P(\omega)$. It is the Fourier transform of the autocorrelation function $p(\tau) = < f(t) f(t + \tau) >$, i.e.,

$$P(\omega) = \int_{-\infty}^{\infty} p(\tau) \ \exp(-i\omega\tau) \ d\tau. \tag{4.3}$$

The symbol $< \ >$ indicates averaging over the time t. (For calculation see also Havskov and Alguacil (2002)). Depending on whether f(t) is a displacement (d), velocity (v) or acceleration (a) record, $P(\omega)$ is given in units m^2/Hz, $(m/s)^2/Hz$ or $(m/s^2)^2/Hz$.
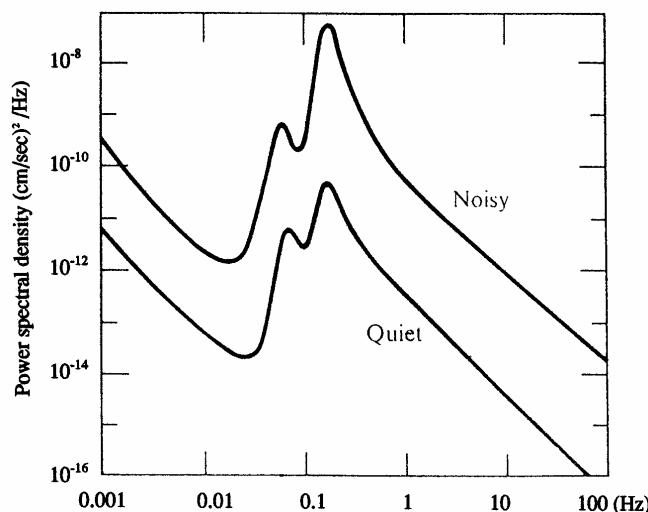
The oscillatory ground-motion x(t) of seismic noise (but also of the harmonic terms of a transient signal) can be approximated by sine-waves $x(t) = a_d \sin\omega t$ with a_d as the displacement amplitude. Therefore, when converting displacements into the related velocities dx/dt or accelerations d^2x/dt^2, we get as the respective velocity and acceleration amplitudes $a_v = a_d \omega$ and $a_a = a_d \omega^2$, respectively. Thus, knowing the displacement power spectral density value $P_d(\omega)$, one can calculate the respective values of the velocity (P_v) or acceleration power spectral density (P_a), i.e.,

$$P_v(\omega) = P_d \ \omega^2 = 4\pi^2 \ f^2 \ P_d \tag{4.4}$$

and

$$P_a(\omega) = P_d \ \omega^4 = 16\pi^4 \ f^4 \ P_d = \ 4\pi^2 \ f^2 \ P_v \tag{4.5}$$
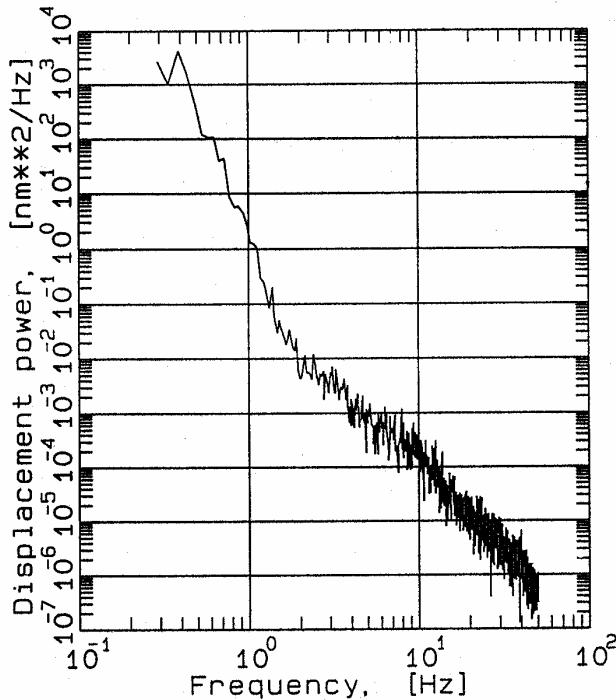
or vice versa. Fig. 4.5 depicts the velocity power spectra of ambient noise at noisy and quiet conditions for a typical station on hard basement rock.


Fig. 4.5 Velocity power spectra of ambient seismic noise at noisy and quiet conditions for a typical station on hard basement rock (reproduced from Aki and Richards 1980; with kind permission of the authors).

An individual displacement power density spectrum as measured at a rather quiet site in NW Iran is depicted in Fig. 4.6.


Fig. 4.6 Spectrum of displacement power spectral density calculated from 6 moving, 50% overlapping intervals of short-period noise records, 4096 samples long each, i.e., from a total record length of about 80 s at a rather quiet site in NW Iran.

As in acoustics, the relative seismic signal or noise power $(a_2/a_1)^2$ is often expressed in units of dB (= deciBel). The power difference in dB is $10 \log[(a_2/a_1)^2] = 20 \log(a_2/a_1)$. When expressing the power spectral density in units of dB referred to 1 $(m/s^2)^2/Hz$, (4.5) can be written as:

$$\mathbf{P_a}[dB] = 10 \log (P_a / 1 \ (m/s^2)^2/Hz). \tag{4.6}$$

Peterson (1993) has presented a new global noise model in these units. It represents the upper- and lower-bound envelopes of a cumulative compilation of representative ground acceleration power spectral densities determined for noisy and quiet periods at 75 digital stations world-wide. The models are commonly referred to as the New High Noise Model (NHNM) and New Low Noise Model (NLNM), respectively (Fig. 4.7) and they represent the currently accepted standard for expected limits of seismic noise. Exceptional cases may exceed these limits, of course.

By substituting the period $T = 1/f$ (in s) for the frequency f in (4.4) and (4.5) , we get:
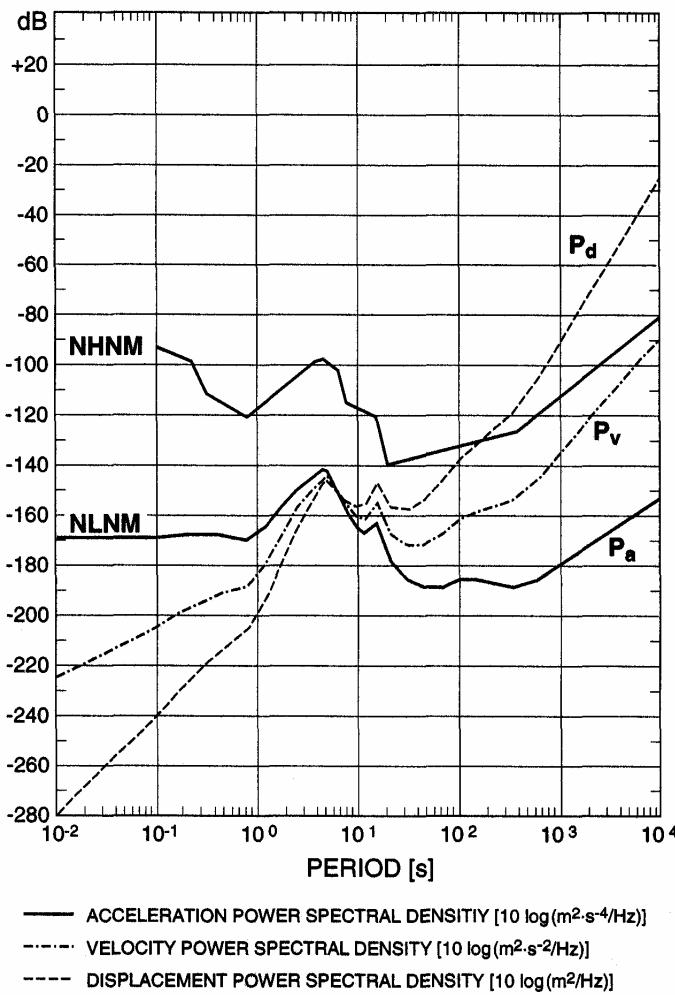
$$\mathbf{P_v}[dB] = \mathbf{P_a}[dB] + 20 \log (T/2\pi) \tag{4.7}$$

and

$$\mathbf{P_d}[dB] \ = \ \mathbf{P_a}[dB] + 40 \log (T/2\pi) = \mathbf{P_v}[dB] + 20 \log (T/2\pi). \tag{4.8}$$

5

Consequently, for the period $T = 2\pi = 6.28$ s $\mathbf{P_a = P_v = P_d}$ (in numbers but not units of dB!). Also, $(\mathbf{P_d - P_a}) = 2 \times (\mathbf{P_v - P_a}) =$ constant for any given period, negative for $T < 2\pi$ and positive for $T > 2\pi$ (Fig. 4.7).


Fig. 4.7 Envelope curves of acceleration noise power spectral density $\mathbf{P_a}$ (in units of dB related to 1 $(m/s^2)^2/Hz$) as a function of noise period (according to Peterson, 1993). They define the new global high (NHNM) and low noise models (NLNM) which are currently the accepted standard curves for generally expected limits of seismic noise. Exceptional noise may exceed these limits. For the NLNM the related curves calculated for the displacement and velocity power spectral density $\mathbf{P_d}$ and $\mathbf{P_v}$ in units of dB with respect to 1 $(m/s)^2/Hz$ and 1 m^2/Hz are given as well (reproduced from Journal of Seismology, 2, 1998, "Conversion and comparability of data presentations on seismic background noise", P. Bormann, p. 39, Fig. 2; © Kluwer Academic Publishers, with permission of Kluwer Academic Publishers).

For periods which define the "corners" of the envelopes of the NLNM and NHNM, Tables 4.1 and 4.2 give the related displacement, velocity and acceleration power density values in their respective kinematic units as well as in dB.

The dynamic range of a seismic recording is also usually expressed in units of dB. According to Fig. 4.7 we would need a seismograph with a dynamic range of about 260 dB in order to cover the noise displacement amplitudes in the period range 10^{-2} to 10^4 s. This is more than the best

currently available high-resolution broadband seismograph can achieve. When recording noise velocity or acceleration instead, the required dynamic range is reduced to about 140 dB and 110 dB, respectively. In the case of analog recordings on paper of about 30 cm width, the minimum double amplitude, which can be resolved visually on the record is about 1 mm and the maximum that can be recorded without clipping is 300 mm. Thus, the dynamic range is $10 \log (300/1)^2 = 20\log (300)$, i.e., only 50 dB. In the case of digital recordings with an n-bit Analog-Digital-Converter (ADC; see Chapter 6) a dynamic range of $6 \times n$ in dB can be covered, i.e., 144 dB with a 24-bit ADC. This corresponds to an equivalent range on an analog recording of amplitudes between 1 mm and 16 km!

The dynamic range of digital seismographs is usually defined via the maximum recordable SNR above the level of ambient noise or instrumental self-noise, allowing for the resolution of noise by a few bits. But because of the differences (discussed above) between coherent transient seismic signals and the largely incoherent random seismic noise, this is not a straight-forward calculation. Below we show how signal and noise amplitudes can be expressed in a comparable way.

Tab. 4.1 Noise power spectral densities at selected periods and in different units which define the new global low-noise model (NLNM) as given by Peterson (1993). Peterson published values for P_a [dB] only. The respective numbers for ground acceleration (P_a), velocity (P_v and P_v) and displacement (P_d and P_d) have been calculated using Eqs. (4.4) to (4.8). Between the given periods the values are linearly interpolated in a PSD-logT diagram.

T [s]	P_a [m^{2}s^{-4}/Hz]	P_a [dB]	P_v [m^{2}s^{-2}/Hz]	P_v [dB]	P_d [m^2/Hz]	P_d [dB]
0.10	1.6×10^{-17}	- 168.0	4.1×10^{-21}	- 203.9	1.0×10^{-24}	- 239.9
0.17	2.1×10^{-17}	- 166.7	1.6×10^{-20}	- 198.1	1.1×10^{-23}	- 229.4
0.40	2.1×10^{-17}	- 166.7	8.7×10^{-20}	- 190.6	3.5×10^{-22}	- 214.6
0.80	1.2×10^{-17}	- 169.2	1.9×10^{-19}	- 187.1	3.2×10^{-21}	- 214.5
1.24	4.3×10^{-17}	- 163.7	1.7×10^{-18}	- 177.8	6.5×10^{-20}	- 191.9
2.40	1.4×10^{-15}	- 148.6	2.0×10^{-16}	- 157.0	3.0×10^{-17}	- 165.3
4.30	7.8×10^{-15}	- 141.1	3.6×10^{-15}	- 144.4	1.7×10^{-15}	- 147.7
5.00	7.8×10^{-15}	- 141.1	4.9×10^{-15}	- 143.1	3.1×10^{-15}	- 145.1
6.00	1.3×10^{-15}	- 149.0	1.1×10^{-15}	- 149.4	1.0×10^{-15}	- 149.8
10.00	4.2×10^{-17}	- 163.8	1.0×10^{-16}	- 159.7	2.7×10^{-16}	- 155.7
12.00	2.4×10^{-17}	- 166.2	8.7×10^{-17}	- 160.6	3.2×10^{-16}	- 155.0
15.60	6.2×10^{-17}	- 162.1	3.8×10^{-16}	- 154.2	2.3×10^{-15}	- 146.3
21.90	1.8×10^{-18}	- 177.5	2.2×10^{-17}	- 166.7	2.6×10^{-16}	- 155.8
31.60	3.2×10^{-19}	- 185.0	7.9×10^{-18}	- 171.0	2.0×10^{-16}	- 156.9
45.00	1.8×10^{-19}	- 187.5	9.1×10^{-18}	- 170.4	4.7×10^{-16}	- 153.3
70.00	1.8×10^{-19}	- 187.5	2.2×10^{-17}	- 166.6	2.8×10^{-15}	- 145.6
101.00	3.2×10^{-19}	- 185.0	9.7×10^{-17}	- 160.9	2.1×10^{-14}	- 136.8
154.00	3.2×10^{-19}	- 185.0	1.8×10^{-16}	- 157.2	1.1×10^{-13}	- 129.4
328.00	1.8×10^{-19}	- 187.5	4.9×10^{-16}	- 153.1	1.3×10^{-12}	- 118.7
600.00	3.5×10^{-19}	- 184.4	3.2×10^{-15}	- 144.8	3.0×10^{-11}	- 105.2
10^4	6.5×10^{-16}	- 151.9	3.5×10^{-14}	- 87.9	4.1×10^{-3}	- 23.8
10^5	4.9×10^{-11}	- 103.1	1.2×10^{-2}	- 19.1	2.6×10^6	+ 65.0

Tab. 4.2 Noise power spectral densities at selected periods and in different units which define the new global high-noise model (NHNM) as given by Peterson (1993). Peterson published values for P_a [dB] only. The respective numbers for ground acceleration (P_a), velocity (P_v and P_v) and displacement (P_d and P_d) have been calculated using Eqs. (4.4) to (4.8). Between the given periods the values are linearly interpolated in a PSD-logT diagram.

T [s]	P_a [m^2s^{-4}/Hz]	P_a [dB]	P_v [m^2s^{-2}/Hz]	P_v [dB]	P_d [m^2/Hz]	P_d [dB]
0.10	7.1×10^{-10}	- 91.5	1.8×10^{-13}	- 127.5	4.5×10^{-17}	- 163.4
0.22	1.8×10^{-10}	- 97.4	2.2×10^{-13}	- 126.5	2.7×10^{-16}	- 155.6
0.32	8.9×10^{-12}	- 110.5	2.3×10^{-14}	- 136.4	6.6×10^{-17}	- 162.2
0.80	1.0×10^{-12}	- 120.0	1.6×10^{-14}	- 137.9	2.6×10^{-16}	- 155.8
3.80	1.6×10^{-10}	- 98.0	5.8×10^{-11}	- 102.4	2.1×10^{-11}	- 106.7
4.60	2.2×10^{-10}	- 96.5	1.2×10^{-10}	- 99.2	6.4×10^{-11}	- 101.9
6.30	7.9×10^{-11}	- 101.0	8.0×10^{-11}	- 101.0	7.9×10^{-11}	- 101.0
7.90	4.5×10^{-12}	- 113.5	7.1×10^{-12}	- 111.5	1.4×10^{-11}	- 109.5
15.40	1.0×10^{-12}	- 120.0	6.0×10^{-12}	- 112.2	3.6×10^{-11}	- 104.4
20.00	1.4×10^{-14}	- 138.5	1.4×10^{-13}	- 128.4	1.4×10^{-12}	- 118.4
354.80	2.5×10^{-13}	- 126.0	8.0×10^{-10}	- 91.0	2.6×10^{-6}	- 55.9
10^4	9.7×10^{-9}	- 80.1	2.5×10^{-2}	- 16.1	6.2×10^4	+ 47.9
10^5	1.4×10^{-5}	- 48.5	3.6×10^3	+ 35.5	9.0×10^{11}	+ 119.6

4.1.3 Conversion of spectral amplitudes or power densities into recording amplitudes

According to Aki and Richards (1980) the *maximum* amplitude of a wavelet f(t) near t = 0 can be *roughly approximated* by the product of the amplitude spectral density and bandwidth of the wavelet, i.e.,

$$f(t)_{t=0} = |F(\omega)| \, 2 \, (f_u - f_l) \qquad (4.9)$$

with f_u and f_l being the upper and lower corner frequencies of the band-passed signal. Likewise, if the power spectral density of noise is defined according to Eq. (4.3) for $-\infty < \omega < +\infty$ then we get for $P(\omega) = P =$ const. for $\omega_l < |\omega| < \omega_u$ and $P(\omega) = 0$ otherwise, the *mean square amplitude* of noise in the time domain is

$$< f^2(t) > = 2P \, (f_u - f_l). \qquad (4.10)$$

Thus, the power spectral density (PSD) must be integrated over the passband of a filter to obtain the power (or *mean square amplitude*) at the output of the filter. The square root of this power is then the *root mean square* (RMS) or effective filter amplitude

$$a_{RMS} = \{2P \times (f_u - f_l)\}^{1/2} \qquad (4.11)$$

Therefore, specifying seismic noise by its RMS amplitudes is meaningless without definition of the bandwidth. If, however, the noise power P is not computed according to the

mathematical approach based on complex notation but from positive frequencies only (so-called engineering approach; see Chapter 5 and explanations given to Eqs. (5.4) and (5.5)) then we obtain $P = 2P$ because of $P(-\omega) = P(+\omega)$, and accordingly

$$a_{RMS} = \{P \times (f_u - f_l)\}^{1/2}. \tag{4.12}$$

Note: The values given by **the NLNM and NHNM** in Fig. 4.7 and Tabs. 4.1 and 4.2, respectively, are in fact $P = 2P$, i.e., they **represent already the total power**. Calculating RMS amplitudes by inserting incorrectly P into Eq. (4.11) would yield values which are 3dB larger then those calculated by using (4.12). So one should make sure beforehand, which definition of power has been used to calculate the PSD. For consistency we will refer in the following only to (4.12).

From (4.12) it follows that the calculated a_{RMS} amplitudes increase with the absolute bandwidth. Therefore, signal and noise amplitudes can be made commensurate only when plotting them in a *constant relative bandwidth* (**RBW**) over the whole frequency range. The RBW can be expressed by a number or in terms of octaves or decades. Increasing the frequency of a signal by one octave means doubling its frequency, and by one decade multiplying it by ten. Accordingly, a band-passed signal (or filter) with n octaves or m decades has a corner frequency ratio

$$f_u/f_l = 2^n = 10^m \tag{4.13}$$

and a (not arithmetic but geometric!) *center frequency* f_o of

$$f_o = (f_u \times f_l)^{1/2} = f_l \times 2^{n/2} = f_l \times 10^{m/2} \ . \tag{4.14}$$

From this follows for the *relative bandwidth*

$$\mathbf{RBW} = (f_u - f_l)/f_o = (2^n - 1)/2^{n/2} = (10^m - 1)/10^{m/2} \tag{4.15}$$

and (4.12) can be written as

$$a_{RMS} = \{P \times (f_u - f_l)\}^{1/2} = (P \times f_o \times \mathbf{RBW})^{1/2} \tag{4.16}$$

Octaves n can be converted easily into decades m and vice versa by using the relation

$$m = \log(f_u/f_l) = n \log 2 \tag{4.17}$$
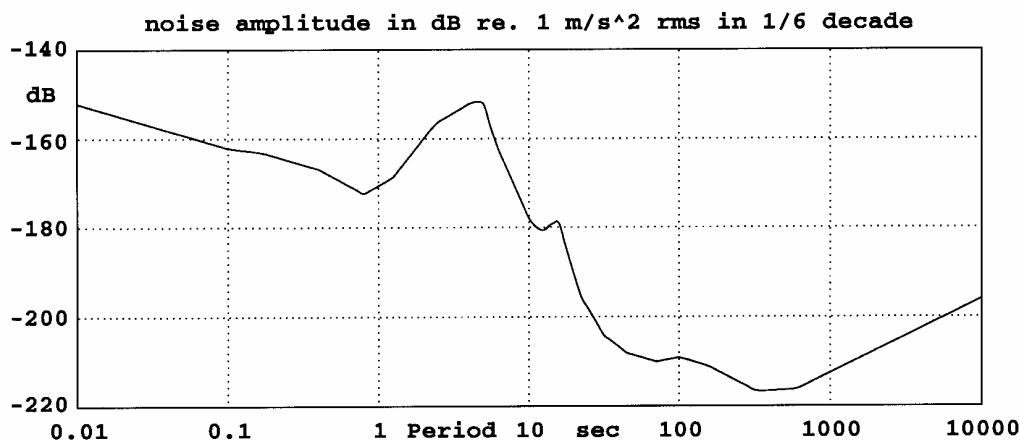
where $n = \log(f_u/f_l)/\log 2$. According to Eq. (4.15) the relative bandwidth for a 1 octave filter is 0.7071 and for a 2/3 octave filter 0.466. Aki and Richards (1980, vol.1, p. 498) converted PSD into ground motions by putting the bandwidth of the noise signal at half the considered (center) frequency, i.e., by assuming $f_u - f_l = 0.5\, f_o$. This correspons to an RBW of roughly 2/3 octave. By using the definition of power on which Eq. (4.11) is based they obtained $a_{RMS} = (P \times f_o)^{1/2}$.

Other authors (e.g., Fix, 1972; Melton, 1978) have used an integration bandwidth of 1/3 octave (a standard bandwidth in acoustics) for computing RMS amplitudes from PSD. Melton reasoned that this is nearly ±10% about the center period in width and thus close to the tolerance with which an analyst can measure the period on an analog seismogram. Therefore, using a 1/3 octave bandwidth seemed to him a reasonable convention for calculating RMS noise amplitudes from PSD. The differences, as compared to RMS values based on 1/4 or 1/2 octave bandwidths, are less than 20%. But 1/3 octave amplitudes will be only about 70% or 50% of the respective RMS

amplitudes calculated for 2/3 or 4/3 octave bandwidth, respectively. Typical response curves of short-period narrowband analog seismographs for recording of transient teleseismic body-wave onsets have bandwidths between about 1 and 2 octaves. Choosing a constant one-octave filter bandwidth for comparing amplitudes of noise and transient seismic signals seems to be rather appropriate therefore.

Fig. 4.8 depicts the a_{RMS} noise amplitudes of ground acceleration in a constant bandwidth of 1/6 decade corresponding to the NLNM shown in Fig. 4.7 while Fig. 7.49 in Chapter 7 gives the dynamic range of STS1 and STS2 (see DS 5.1) seismometers above their level of instrumental noise and in relation to the NLNM for RMS amplitudes calculated with 1/3 octave bandwidth. 1/6 decade bandwidth means between 82.5% and 121% of the central frequency f_o. The corresponding values for 1/3 octave are between 89.1% and 112.4% of f_o.

noise amplitude in dB re. 1 m/s^2 rms in 1/6 decade

Fig. 4.8 The USGS New Low Noise Model, here expressed as RMS amplitudes of ground acceleration in a constant relative bandwidth of one-sixth decade (courtesy of E. Wieland).
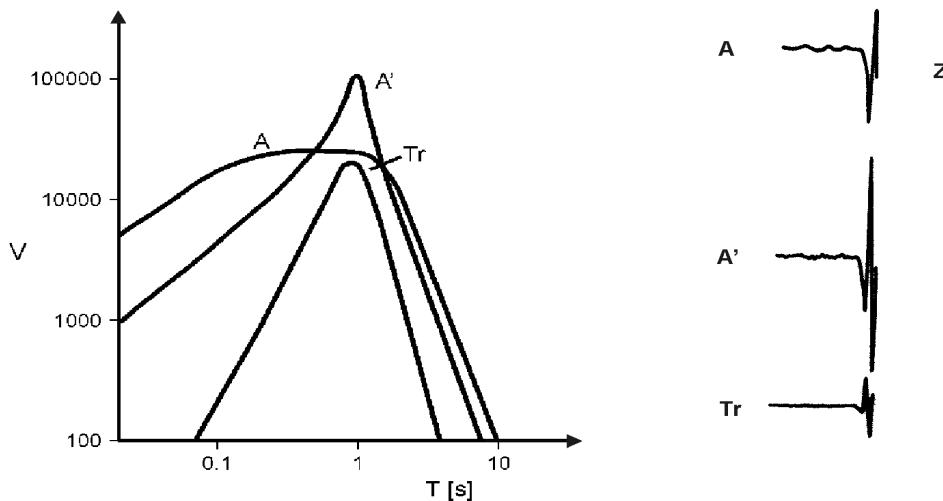
For a_{RMS} determined according to (4.12) or (4.16) there is a 95% probability that the *instantaneous peak* amplitudes of a random wavelet with a Gaussian amplitude distribution will lie within a range of $2a_{RMS}$. Peterson (1993) showed that both broadband and long-period noise amplitudes follow closely a Gaussian probability distribution. In that case the absolute peak amplitudes of the narrowband filtered signal envelopes should follow a Rayleigh distribution. In the case of an ideal Rayleigh distribution the theoretical *average peak amplitudes* (APA) are 1.253 a_{RMS}. From test samples of narrowband filtered VBB and LP noise records Peterson (1993) measured APA values between 1.194 and 1.275. Therefore, RMS amplitudes in 1/6-decade bandwidth correspond approximately to average peak amplitudes in 1/3 octave bandwidth. An example: According to Fig. 4.8 the minimum vertical ground noise between 10 and 20 s is at -180 dB relative to $1m/s^2$. This corresponds to average peak amplitudes of $10^{-180/20}$ $m/s^2 = 1$ nm/s^2 in 1/3 octave bandwidth. Accordingly, the total average peak amplitude in this one octave band between 10 and 20 s is $\sqrt{3}$ nm/s^2.

PD 4.1 in Volume 2 offers an interactive program NOISECON which converts noise specifications into all kinds of standard and non-standard units and compares them to the USGS NLNM, whereas EX 4.1 gives exercises for calculating RBWs and transforming PSDs into a_{RMS} for various kinematic units and bandwidths. It is complemented by several exercises combining eye-estimates and NOISECOM applications for interpreting and converting noise spectra.

4.2   Peculiarities of signal appearance in seismic records

4.2.1   Influence of the seismograph response: Empirical case studies

Fig. 4.9 shows recordings of a real earthquake P-wave onset in different short-period recordings with 1-Hz seismometers.
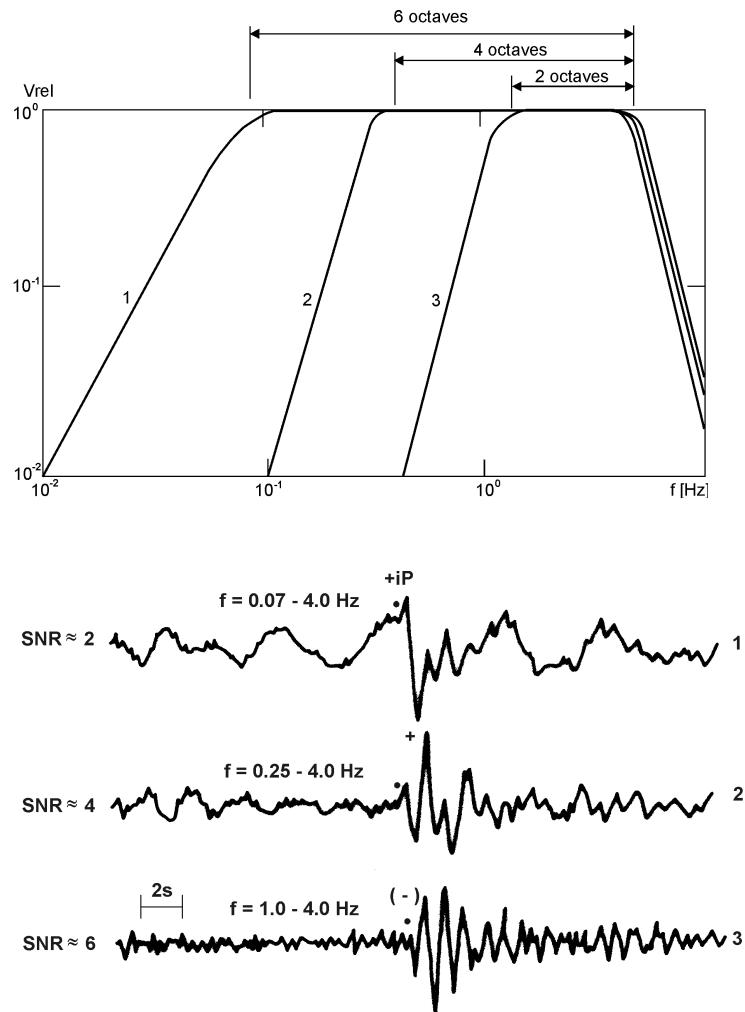

Fig. 4.9 Left: Displacement amplitude magnification curves of three types of short-period seismographs at seismic station MOX with 1/2 octave (type A´), one octave (Tr - trigger seismograph) and four octave bandwidth (type A), respectively; right: records with these seismographs of a P-wave onset of a deep earthquake at an epicentral distance of 72.3° and hypocentral depth of 544 km.

While in recordings of type A with 4 octave bandwidth, the first half cycle contains the largest amplitude, the maximum amplitude in records with 1/2 octave (type A´) and one octave bandwidth (type Tr) is reached only at the third half-swing. Also, the first motion amplitude in the one octave record Tr is strongly reduced as compared to that in record A with four octave bandwidth, despite having nearly the same peak magnification. Accordingly, we have to consider that in narrowband records of high magnification (as with WWSSN short-period seismographs; bandwidth about 1.5 octaves) the reduced first motion amplitudes might get lost in the presence of noise. Since reliable first motion polarity readings are crucial for the determination of fault plane solutions and discriminating earthquakes from explosions, narrowband recordings might result in an unacceptable loss of primary information. Examples are given in Figs. 4.10 and 4.35. With broadband digital recording, this is now less of a problem.

Also note: The maximum amplitude of the P-wave onset in Tr of Fig. 4.9 is only about ½ of that in record A although both have about the same peak magnification at 1 Hz for steady-state harmonic oscillations! And in record A´ the maximum amplitude is only twice as large, even though the A' instrument has four times larger peak amplification than instrument A. This systematic underestimation of amplitudes of transient body-wave onsets of short duration in narrowband records - and thus of related magnitude estimates - has been a matter of considerable debate between the American and Russian delegations in the early Geneva

11
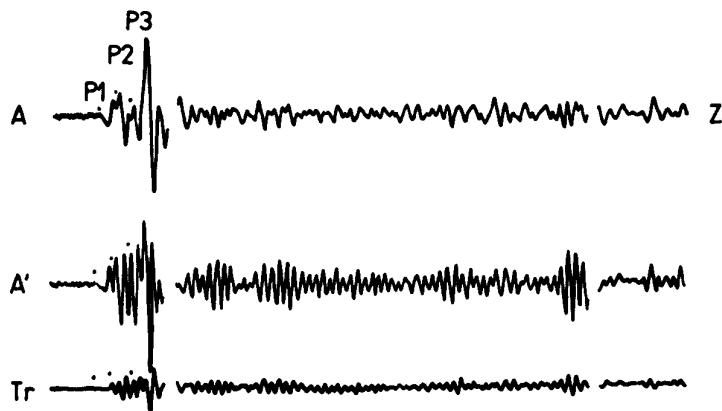
talks to achieve a Comprehensive Nuclear-Test-Ban Treaty (CTBT). In the Soviet Union standard seismographs with amplitude characteristics of type A (2 to 4 octaves) and broadband characteristics of type Kirnos with about 7 octaves bandwidth were used to determine body-wave magnitudes, while American-designed WWSSN stations determined body-wave magnitudes based only on their narrowband short-period standard records of 1.5 octaves bandwidth. A consequence of these differences in magnitude determination was that the American delegation reported a much larger number of weak, unidentified seismic events per year than the Soviet delegation and therefore felt that they required hundreds of U.S. unmanned stations on Soviet territory as well as the possibility for on-site inspections. This blocked, amongst other reasons, the agreement on a comprehensive test-ban treaty for two decades. Today these problems are more of historical interest since the analyst using digital broadband data can shape the filters any way desired. But it still remains a problem to exactly define what filter to use, and analysts should be aware therefore of the filter effects.
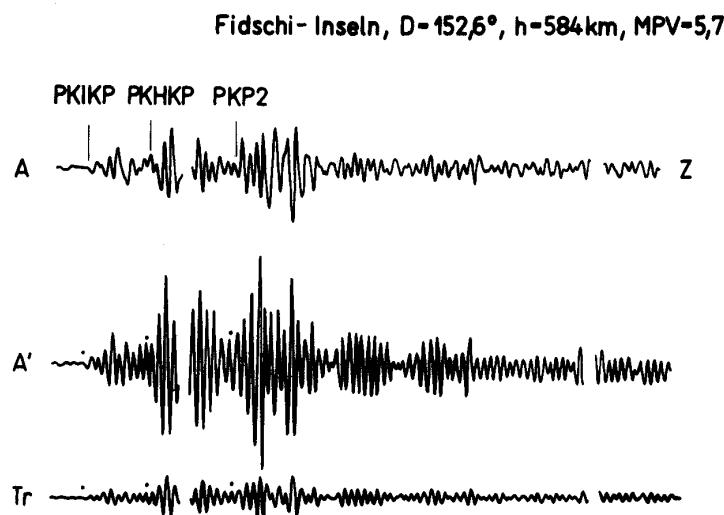
Fig. 4.10 A medium-period velocity-proportional digital broadband record (bandwidth almost 6 octaves between 0.07 – 4 Hz;) at station MOX of an underground nuclear explosion at the Nevada test site (record trace 1) has been filtered with a 4-octave and 2-octave bandpass filter (record traces 2 and 3). The positive first motion (to be expected from an explosion!) is clearly to be seen in the BB record despite of the low SNR, but it is buried in the noise of the 2 octave record despite the general SNR improvement due to narrowband filtering. Note that the different absolute amplitude levels in the three records have all been normalized to the same peak amplitude.

12

The narrower the record bandwidth is, the longer and more oscillating the recorded wavelet of a transient onset becomes. This makes it difficult to recognize, in narrowband records, secondary onsets following closely behind the first one, e.g., onset sequences due to a multiple earthquake rupture (Fig. 4.11), depth phases in the case of shallow earthquakes or branching/crossing of travel-time curves (see Chapter 2 and Fig. 4.12). But the identification and proper time picking of such closely spaced secondary arrivals is crucial for a better understanding of the rupture dynamics, for improved estimates of hypocenter depth or for studies of the fine structure of the Earth.

Fig. 4.11 Short-period records of station MOX of a multiple rupture event at Honshu (D = 88.0°) with different amplitude response characteristics according to Fig. 4.9 left.
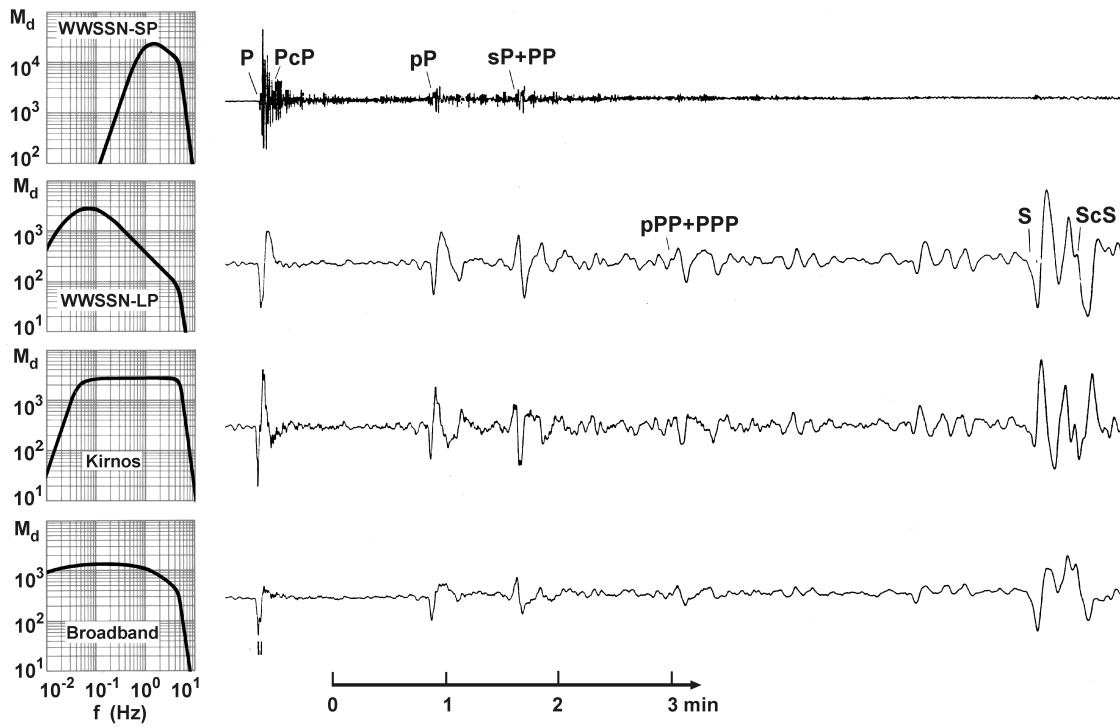
Fig. 4.12 Short-period records of station MOX of a sequence of core phases corresponding to the travel-time branches PKPdf (PKIKP), PKPbc (PKHKP) and PKPab (PKP2) (see Chapter 11) with different amplitude response characteristics according to Fig. 4.9 left.

It is crucial, therefore, to record seismic signals with as large a bandwidth and with as high a linearity, resolution and dynamic range as possible, thus preserving the primary information with least distortion. Filtering should only be applied afterwards, as required for special purposes. With feedback-controlled broadband seismometers and digital data loggers with 24 bit ADCs being readily available, this is no longer a problem (see Chapters 5 and 6). In Fig.

13

4.13 it is clearly recognizable that in the displacement-proportional broadband record of about 10 octaves bandwidth the P-wave onset looks rather simple (negative impulse with only slight positive overswing of the second half-cycle). Its appearance resembles the expected source displacement pulse in the far field (see Fig. 2.4).


Fig. 4.13 Records of a deep earthquake (h = 570 km, D = 75°) at the Gräfenberg Observatory, Germany. They have been derived by filtering a velocity-proportional digital broadband record (passband between 0.05 and 5 Hz) according to the response curves of some traditional standard characteristics (WWSSN_SP and LP, Kirnos) while the bottom trace shows the result of computational restitution of the (nearly real) true ground displacement by extending the lower corner period T_o well beyond 100s (see text) (from Buttkus, 1986).
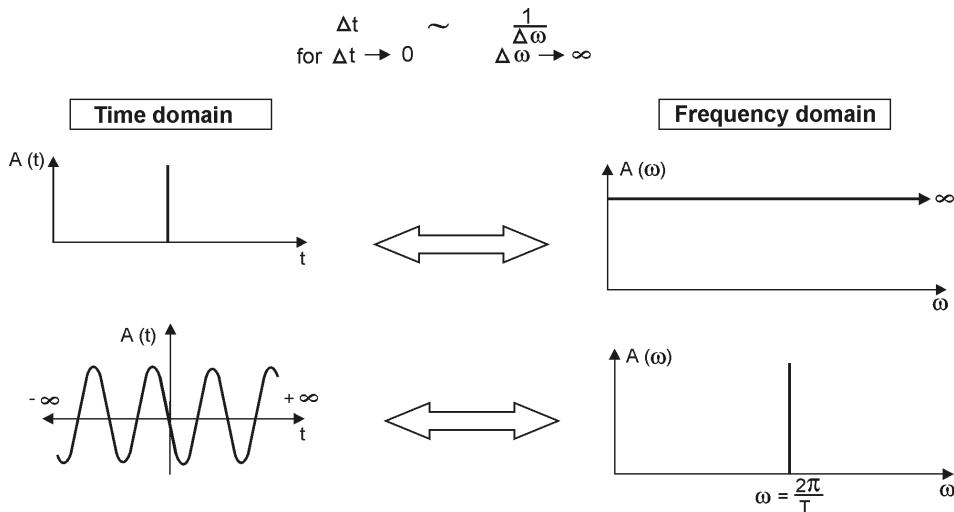
4.2.2 Theoretical considerations on signal distortion in seismic records

The basic theory of seismometry is outlined in Chapter 5. For a more comprehensive introduction to general filter theory and its applications in digital seismology (with exercises) see "Of Poles and Zeros: Fundamentals of Digital Seismology" by Scherbaum (second edition, 2001). The book is accompanied by a CD-ROM "Digital Seismology Tutor" by Schmidtke and Scherbaum (2001; http://www.uni-potsdam.de/u/Geowissenschaft/Software/software.html), which is a very versatile tutorial tool for demonstrating signal analysis and synthesis. Therefore, we will not dwell on it further, however, we will illustrate by way of example some of the essential effects of signal distortion by the transfer function of the seismograph. Signal distortion due to wave propagation effects in the Earth and ways how to eliminate at least some of them are discussed in Chapter 2.
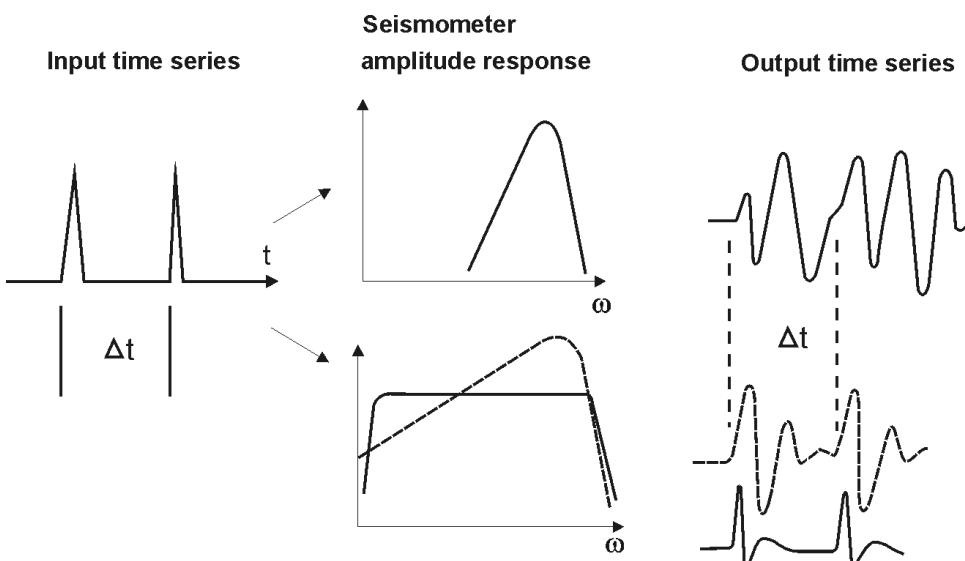
The essence of Eq. (4.1) and Fig. 4.2 is the following: A Dirac (or needle) impulse (see section 5.2.4) in the time domain is equivalent to an infinite homogeneous ("white") spectrum

in the frequency domain. Thus, if the far-field seismic source pulse comes close to a needle impulse of very short duration (e.g., an explosion) we would need in fact a seismograph with (nearly) an infinite bandwidth in order to be able to reproduce this impulse-like transient signal. On the other hand, an infinite monochromatic harmonic signal corresponds to just one spectral line in the frequency spectrum, or, the other way around, if the input signal is a needle impulse with an infinite spectrum but the bandwidth of the seismograph is extremely narrow ($\rightarrow 0$), then the record output would not be a needle impulse at all but rather (after the transient response is over) an (almost) un-attenuated infinite monochromatic record. Fig. 4.14 depicts these extreme cases and Fig. 4.15 sketches seismographic recordings of an impulse sequence with different response characteristics.

Fig. 4.14 Sketch of the equivalent representation of a needle impulse (above) and a stationary infinite monochromatic harmonic signal (below) in the time and frequency domain.
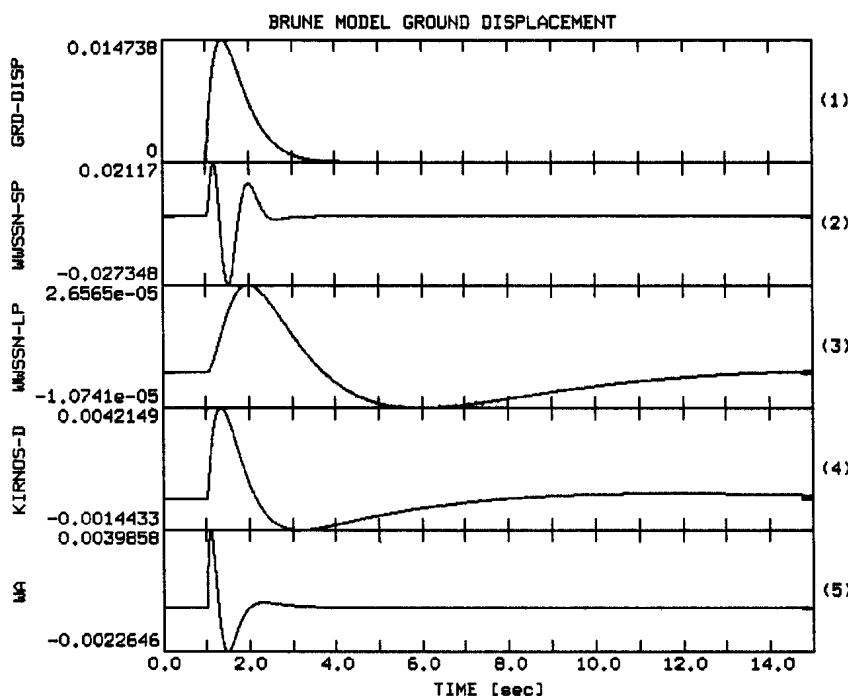
Fig. 4.15 Schematic illustration of the appearance of a sequence of seismic input impulses in record outputs of seismographs with narrow-band displacement response (uppermost trace) and broadband responses (below; broken line – velocity response, full line – displacement response).

According to theoretical considerations by Seidl and Hellweg (1988), the seismometer period T_o has to be about 100 times larger than the duration τ_s of the source-time input function when the source signal shape and its "signal moment" (area under the impulse time curve) is to be reproduced with a relative error < 8 %. As a rule of thumb, these authors state that the relative error is less than about 10% if $T_o > 20\,\pi\,\tau_s$. This means that extreme long-period seismographs would be required to reproduce with sufficient accuracy the displacement impulse of strong seismic events. By "signal restoration" (i.e., instrument response correction or "deconvolution") procedures (Seidl, 1980; Seidl and Stammler, 1984; Seidl and Hellweg, 1988; Ferber, 1989) the eigenperiod of long-period feedback seismometers such as STS1 (T_o = 360 s) and STS2 (T_o = 125 s) can be computationally extended - in the case of high signal-to-noise ratio - by a factor of about 3 to 10 times, and thus the very low-frequency content of the signals can be retrieved. Simulations of standard frequency responses from BB records are available in some of the software packages for signal pre-processing (e.g., PREPROC, Plešinger et al. 1996) or seismogram analysis (e.g., SEISAN, Havskov and Ottemöller, 1999 b; see http://www.ifjf.uib.no/seismo/software/seisan.html/; and Seismic Handler by K. Stammler; see http://www.szgrf.bgr.de/sh-doc/index.html).

Fig. 4.16 shows the very different response of three standard seismograph systems of different damping and bandwidth to a synthetic ground displacement input according to the Brune model of earthquake shear dislocation. The response has been simulated by using the PITSA seismological analysis software (Scherbaum and Johnson, 1992; and http://www.uni-potsdam.de/u/Geowissenschaft/Software/software.html). For the amplitude response of the seismographs of type Wood-Anderson (WA), Kirnos, WWSSN long-period (LP) and WWSSN short-period (SP) see Fig. 3.11.


Fig. 4.16 Distortion of a synthetic ground displacement signal according to the Brune model of earthquake shear dislocation (top trace) by standard seismograph systems (for their response curves see Fig. 3.11) (from Scherbaum 2001, "Of Poles and Zeros", Fig. 10.2, p. 167; © Kluwer Academic Publishers, with permission of Kluwer Academic Publishers).

16

The strong distortion in narrowband recordings after the transient onsets is due to their pronounced *transient response* (TR). It is due to the time required by the seismometer to achieve the values of frequency-dependent magnification and phase shift determined by its amplitude- and phase-frequency characteristics for steady-state harmonic oscillations (see 5.2, Fig. 5.6 and Figure 1a and b in IS 5.2). In Fig. 4.16, the effect of phase-shift adaptation during the time of transient response is clearly seen, especially in the records of the WWSSN and Wood-Anderson short-period instruments. Accordingly, the period of the first half cycle appears to be much shorter than that of the second and third half cycle. The transient response of the seismometer is $\sim \exp(-D_s T_s\, t)$ with D_s – damping and T_s - eigenperiod of the seismometer and t - time, i.e., TR $\to 0$ for $D_s T_s\, t \to \infty$. Thus, for a short-period seismometer with very low damping (narrow-band resonance characteristic!) it takes a long time before the transient response is over while for seismometers with overcritical damping and/or very large T_s (broadband!) the transient response is rather short and negligible.

Fig. 4.17 compares the response of the same seismographs and of the SRO-LP seismograph with the unfiltered velocity broadband record of the STS2 (see DS 5.1) from an earthquake in the Russia-China border region. The differences in record appearance depending on the response characteristic of the seismograph and the time resolution of the record are striking.
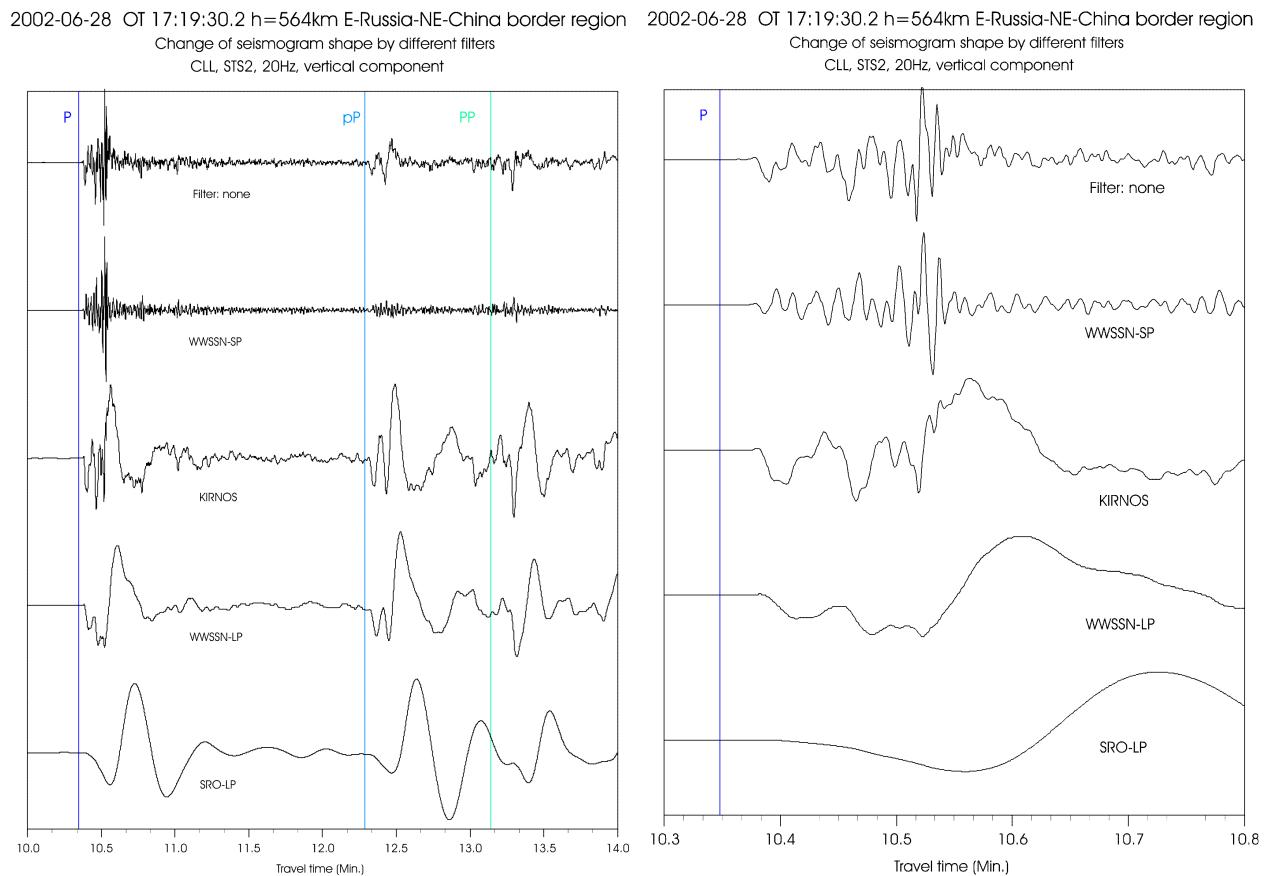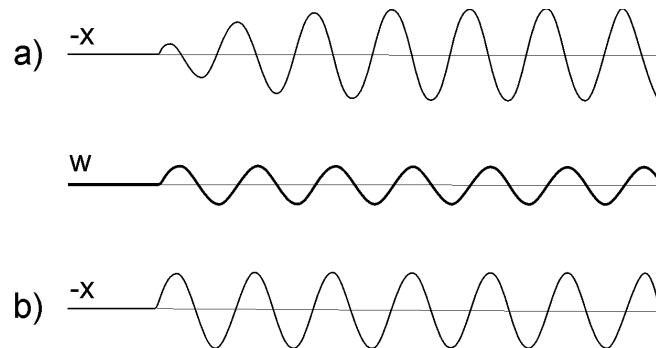

Fig. 4.17 Record segments from an earthquake at the Russia-China border of 4 min (left) and 30 s duration (right). Uppermost traces: unfiltered STS2 velocity broadband seismogram; other traces: filtered records which simulate the seismograms of standard recordings of type WWSSN-SP, Kirnos, WWSSN-LP and SRO-LP (courtesy of S. Wendt).

Fig. 4.18 gives an example from a simulation of seismometer response to a monochromatic harmonic ground motion w(t) of frequency 1 Hz as input. It has been partly made from two different snapshots of an interactive web site demonstration of the Technical University of Clausthal, Germany (http://www.ifg-tu-clausthal.de/java/seis/seisdemo_d.html). Trace a) has been recorded with a seismometer of eigenperiod $T_s = 1$ Hz and damping $D_s = 0.2$ (i.e., resonance at 1 Hz!) while for trace b) $T_s = 20$ s and $D_s = 0.707$. In the first record the transient response takes about 3 s before the steady-state level of constant amplitudes corresponding to the amplitude response of the seismometer and the constant phase shift of about 110° have been reached (after the sixth record half cycle). In record b) the transient response takes less than half a second and the seismometer mass follows the ground motion with practically no phase shift.

Fig. 4.18   Simulation of displacement signal output x(t) (= relative displacement of the seismometer mass) of a spring-mass pendulum seismometer responding to a monochromatic harmonic ground motion w(t) of period T = 1 s (thick line in the middle). a) Displacement output of a seismometer with low damping ($D_s = 0.2$) and eigenperiod $T_s = 1$ s (i.e., resonance); b) Displacement output of a long-period and normally damped seismometer ($T_s = 20$ s; $D_s = 0.707$). For discussion see text.

4.3   Causes and characteristics of ambient seismic noise

4.3.1   Ocean microseisms and ocean bottom noise

Most of the early 20th century seismographs by Wiechert, Mainka, Galizyn, Bosch-Omori, Milne-Shaw and others are medium-period broadband systems. The more sensitive ones with 100 to 500 times magnification of the ground motion were already able to record microseisms around the noise peak at about 6 ± 2 s (see Figs. 4.5 and 4.7). Such recordings were reported by Algue in 1900. Wiechert (1904) proposed at the second international seismological conference that these microseisms are caused by ocean waves on coasts. Later it was found that one must discriminate between: a) smaller primary ocean microseisms with periods around 14 ± 2 s and b) secondary ones related to the main noise peak around 6 s (see Fig. 4.5 and 4.7).

Primary ocean microseisms are generated only in shallow waters in coastal regions. Here the wave energy can be converted directly into seismic energy either through vertical pressure variations, or by the smashing surf on the shores, which have the same period as the water waves ($T \approx 10$ to 16 s) (Fig. 4.19a). Haubrich et al. (1963) compared the spectra of microseisms and of swell at the beaches and could demonstrate a close relationship between

the two data sets. Contrary to this, the secondary ocean microseisms could be explained by Longuet-Higgins (1950) as being generated by the superposition of ocean waves of equal period traveling in opposite directions, thus generating standing gravity waves of half the period. These standing waves cause non-linear pressure perturbations that propagate without attenuation to the ocean bottom. The area of interference X may be off-shore where the forward propagating waves generated by a low-pressure area L superpose with the waves traveling back after being reflected from the coast (Fig. 4.19b). But it may also be in the far deep ocean when the waves, excited earlier on the front side of the low-pressure zone, interfere later with the waves generated on the back-side of the propagating cyclone. Horizontal and vertical noise amplitudes of marine microseisms are similar. The particle motion is of Rayleigh-wave type, i.e., elliptical polarization of the particle motion in the vertical propagation plane. A more detailed discussion on sources and properties of primary and secondary microseisms can be found in Cessaro (1994) and Friedrich et al. (1998).

Fig. 4.19   Schemes for the generation of a) primary and b) secondary microseisms (for explanations see text). L – cyclone low-pressure area, X – area of interference where standing waves with half the period of ocean waves develop (reproduced from Journal of Seismology, 2, 1, 1998, "Ocean-generated microseismic noise located with the Gräfenberg array"; Friedrich, Krüger & Klinge, p. 62, Fig. 12; © Kluwer Academic Publishers, with permission of Kluwer Academic Publishers).
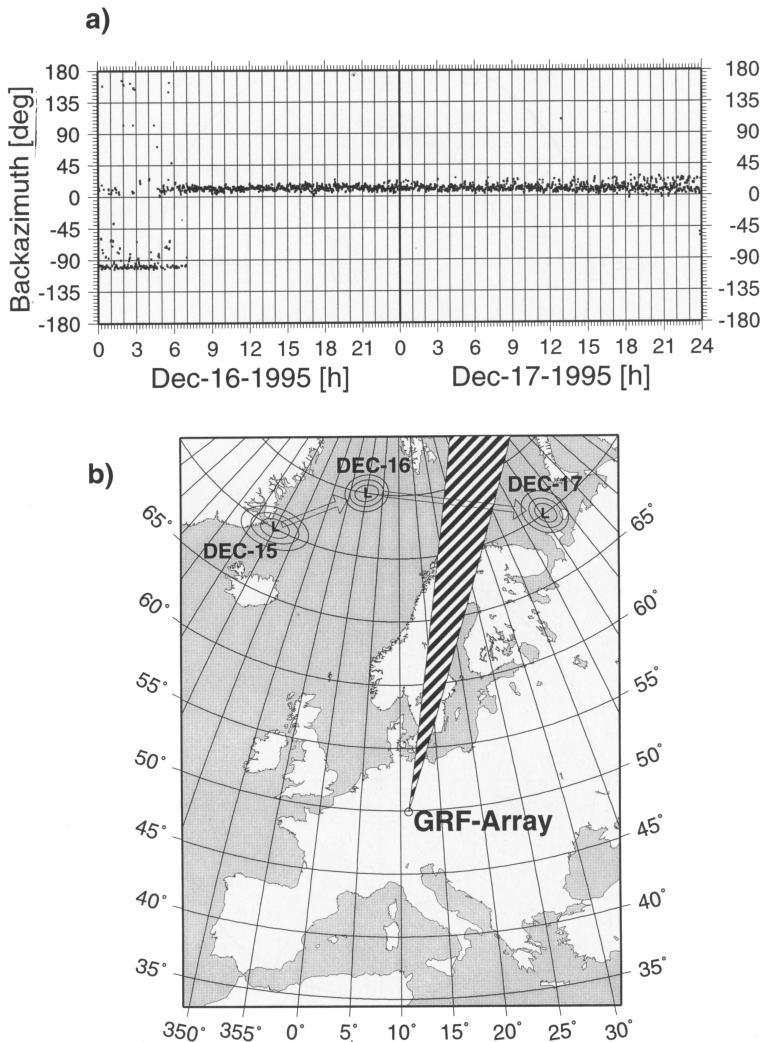
Note that the noise peak of secondary microseisms has a shorter period when generated in shallower inland seas or lakes (T ≈ 2 to 4 s) instead of in deep oceans. Also, off-shore interference patterns largely depend on coastal geometries and the latter may allow the development of internal resonance phenomena in bays, fjords or channels (see Fig. 4.20 which affect the fine spectrum of microseisms. In fact, certain coastlines may be distinguished by unique "spectral fingerprints" of microseisms.

fjord   rectangular coast   channel

Fig. 4.20 Examples for coastline geometries that provide suitable interference conditions for the generation of secondary microseisms (reproduced from Journal of Seismology, 2, 1, 1998, "Ocean-generated microseismic noise located with the Gräfenberg array"; Friedrich, Krüger & Klinge, p. 63, Fig. 13; © Kluwer Academic Publishers, with permission of Kluwer Academic Publishers).

Medium-period ocean/sea microseisms experience low attenuation. They may therefore propagate hundreds of km inland. Since they are generated in relatively localized source areas, when looked at from afar they have - despite the inherent randomness of the source process - a rather well developed coherent portion, at least in the most energetic and prominent component. This allows one to locate the source areas and track their movement by means of seismic arrays (e.g., Cessaro, 1994; Friedrich et al., 1998; Fig. 4.21). This possibility has already been used decades ago by some countries, e.g., in India, for tracking approaching monsoons with seismic networks under the auspices of the Indian Meteorological Survey, although Cessaro (1994) showed that the primary and secondary microseism source locations do not follow the storm trajectories directly. While near-shore areas may be the source of both primary and secondary microseisms, the pelagic sources of secondary microseisms meander within the synoptic region of peak storm wave activity.

In recent years more and more ocean-bottom seismographs (OBS; see, e.g., Havskov and Alguacil) have been deployed in order to overcome the inhomogeneous distribution of land-based seismic stations. But permanent OBS installations are still rare. Generally, the noise level at the ocean bottom, even in deep seas, is higher than that on land (by about 10 to 30 dB) and increases with higher frequencies (e.g., Bradner and Dodds, 1964). On the ocean bottom, as on land, the secondary microseism noise peak between 0.1 and 1 Hz dominates. Background noise levels in this frequency range tend to be higher in the Pacific than in the Atlantic because of its larger size and its general weather conditions. While short-period body-wave arrivals around 1 Hz have been clearly recorded during calm-weather periods by OBSs in the North Atlantic, even at teleseismic distances, they are recognizable in OBS records in the Pacific only for very large events at distances of less than a few tens of degrees. On the other hand, long-period P, S and surface waves are consistently well recorded by OBSs in the noise minimum between about 0.03 and 0.08 Hz for magnitudes 6 ± 0.3 even at distances D > 100° (Blackman et al., 1995).

a)

b)

Fig. 4.21 An example of good coherence of medium-period secondary ocean microseisms at a longer distance from the source area which, in this case, allows rather reliable determinations of the backazimuth of the source area by f-k analysis with seismic arrays (see Chapter 9). Figure a) above shows how the backazimuth determination changed from one day to the next, while b) shows the location of the two storm areas and the seismic array. Observations by at least two arrays permit localization and tracking of the noise-generating low-pressure areas (reproduced from Journal of Seismology, 2, 1, 1998, "Ocean-generated microseismic noise located with the Gräfenberg array"; Friedrich, Krüger & Klinge, p. 55, Fig. 7; © Kluwer Academic Publishers, with permission of Kluwer Academic Publishers).

4.3.2 Short-period seismic noise
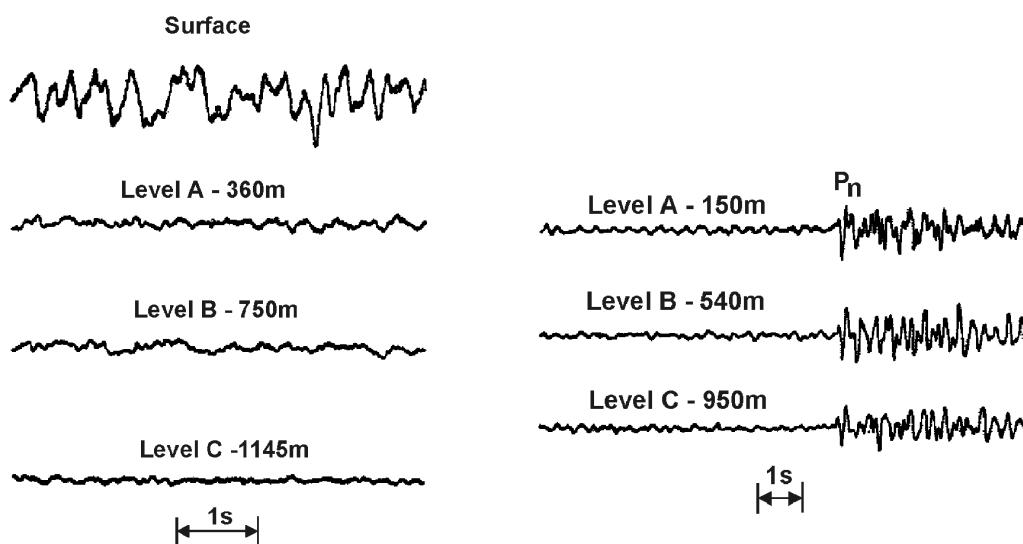
Short-period seismic noise may have natural causes such as wind (wind friction over rough terrain; trees and other vegetation or built-up objects swinging or vibrating in the wind), rushing waters (waterfalls or rapids in rivers and creeks) etc. Wind-generated noise is broadband, ranging from about 0.5 Hz up to about 15 to 60 Hz (Young et al., 1996). But the dominant sources of high-frequency noise are man-made (rotating or hammering machinery, road and rail traffic etc.; see Chapter 7.). Most of these sources are distributed, stationary or moving. Their contributions, coming from various directions, superpose to a rather complex,
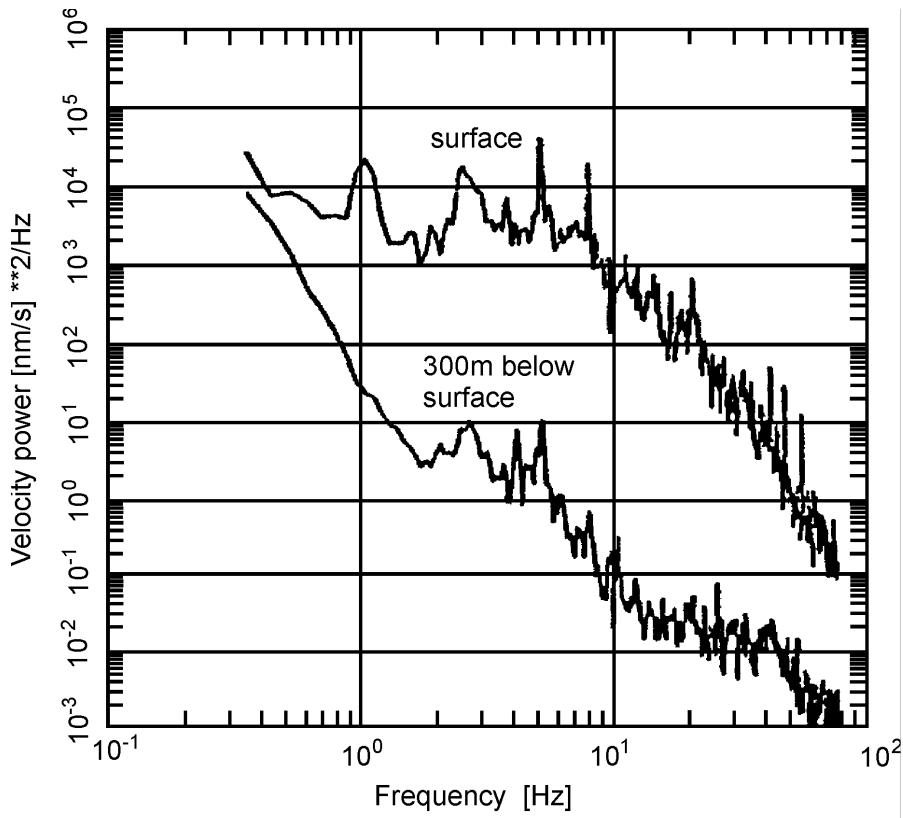
more or less stationary random noise field. The particle motion of short-period noise is therefore more erratic than for long-period ocean noise. Nevertheless, polarization analysis, averaged over moving time-windows, sometimes reveals preferred azimuths of the main axis of horizontal particle motion hinting at localized noise sources. Also the vertical component is clearly developed and averaged particle motion in 3-component records indicates fundamental Rayleigh-wave type polarization. A rather popular and cost-effective microzonation method is based on this assumption. It derives information about the fundamental resonant frequency of the soft-soil cover and estimates local site amplification of ground motion from the peak in the horizontal to vertical component spectral noise ratio (*Nakamura method*, e.g., Nakamura, 1989; Bard, 1999).

Because of the surface-wave character of short- and medium-period noise, the horizontal propagation velocity of seismic noise is frequency dependent. It is close to the shear-wave velocity in the uppermost crustal layers (about 2.5 to 3.5 km/s for outcropping hard rock and about 300 to 650 m/s for unconsolidated sedimentary cover). This is rather different from the apparent horizontal propagation velocity of P waves and all other steeply emerging teleseismic body-wave onsets.

The surface-wave nature of seismic noise (including ocean noise) is also the reason for the exponential decay of noise amplitudes with depth, which is not the case for body waves (Fig. 4.22). Since the penetration depth of surface waves increases with wavelength, high frequency noise attenuates more rapidly with depth. In the case of Fig. 4.23, the noise power at 300 m depth in a borehole was reduced, as compared to the surface, by about 10 dB, at f = 0.5 Hz, 20 dB at 1 Hz and 35 dB at 10 Hz. Withers et al. (1996) found that for frequencies between 10 to 20 Hz, the SNR could be improved between 10 to 20 dB and for f between 23 and 55 Hz as much as 20 to 40 dB by deploying a short-period sensor at only 43 m below the surface. But both noise reduction as well as signal behavior with depth depend also on local geological conditions (see 4.4.5).
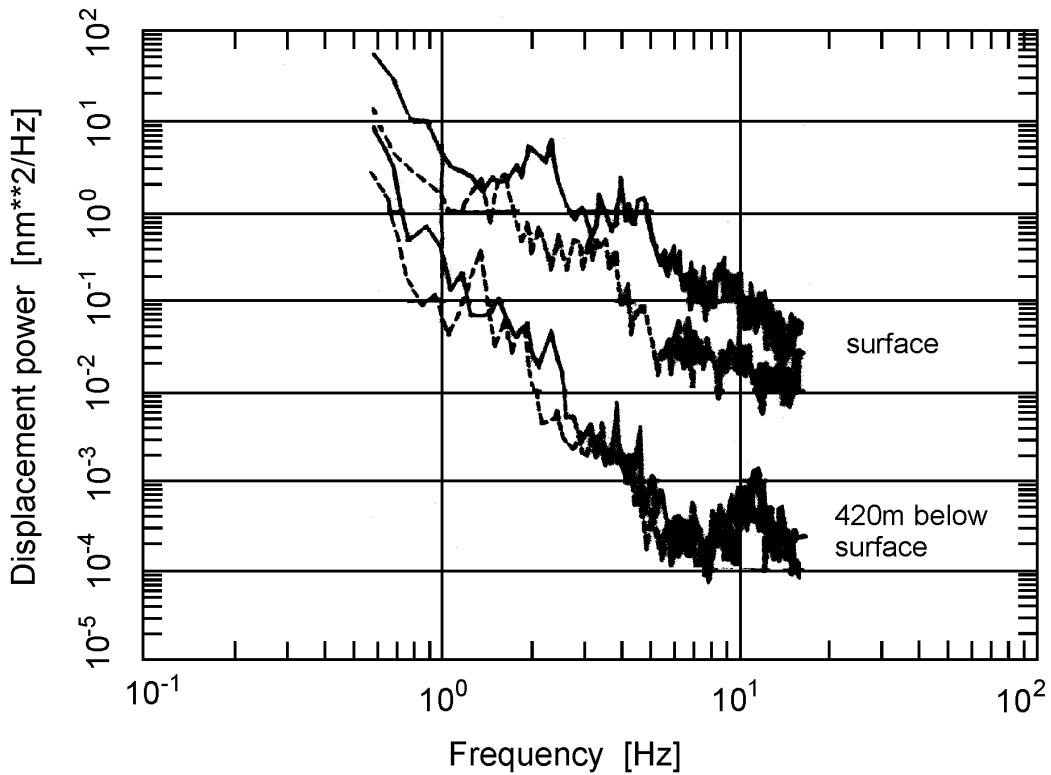

Fig. 4.22 Recording of short-period seismic noise (left) and signals (right) at the surface and at different depth levels of a borehole seismic array (modified from Broding et al., 1964).

Fig. 4.23 Velocity power density spectra as obtained for noise records at the surface (top) and at 300 m depth in a borehole (below) near Gorleben, Germany (courtesy of M. Henger).

Signals which have small phase shifts and identical time dependence and polarization, so that they can interfere constructively, are termed coherent. This is usually the case for seismic signals generated and radiated by a common source process. The degree of coherence is defined by the ratio between the auto- and the cross-correlation of the time series. It may vary between 0 and 1. For seismic noise it shows a distinct frequency dependence. Coherence may be rather high for long-period ocean microseisms (> 70 %) while it drops usually below 30% for f > 1 Hz. Accordingly, the correlation radius, i.e., the longest distance between two seismographs for which the noise recorded in certain spectral ranges is still correlated, increases with the noise period. It may be several km for f < 1 Hz but drops to just a few tens of meters or even less for f > 50 Hz. For seismic noise, it is usually not larger than a few wavelengths.

Generally, there is a good correlation between increased noise levels and higher wind speeds. While for wind speeds below 3 to 4 m/s, one may observe omni-directional background noise coherent at frequencies below 15 Hz, this coherence is destroyed at higher wind speeds with increased air turbulence (Withers et al., 1996). Amplitudes of wind noise are apparently nonlinear. Wind noise increases dramatically at wind speeds greater than 3 to 4 m/s and may reach down to several hundred meters below the surface at wind speeds > 8 m/s (Young, 1996). But generally, the level and variability of wind noise is much higher at or near the surface and is reduced significantly with depth (Fig. 4.24).

23
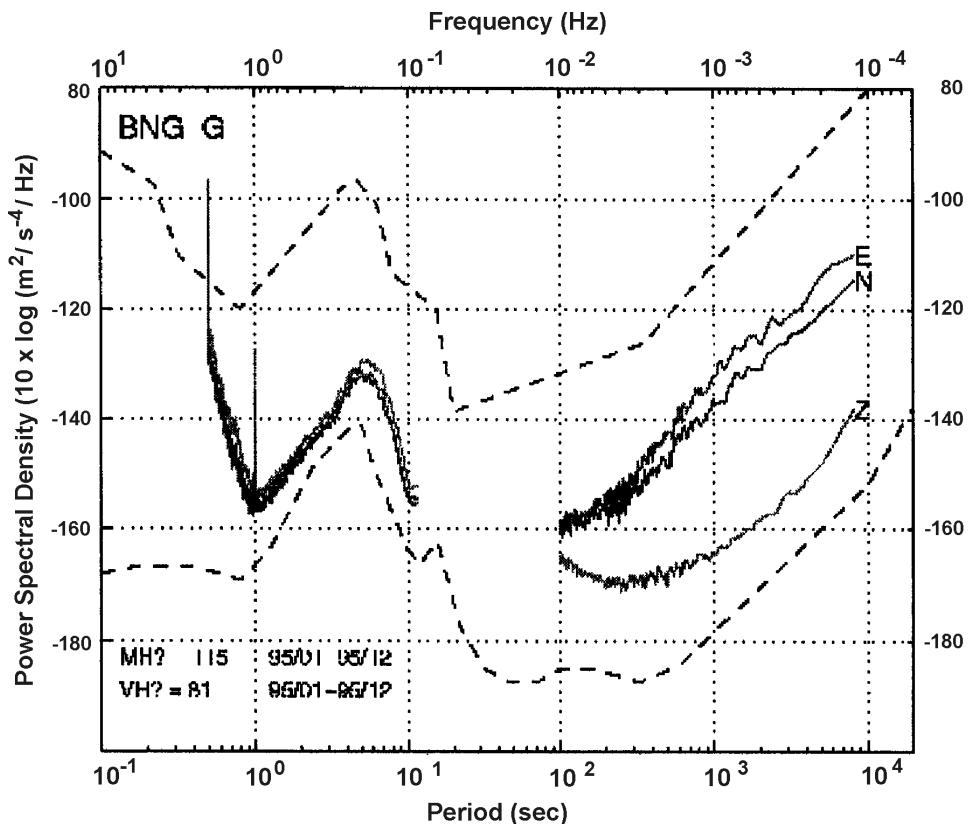
Fig. 4.24 Displacement power noise spectra measured at the surface (upper curves) and at 420 m below the surface in a disused salt mine at Morsleben, Germany (lower curves) on a very quiet day (hatched lines) and on a day with light wind on the surface (wind speed about 4 m/s; full lines).

Thus, differences in the frequency spectrum, horizontal wave-propagation velocity, degree of coherence and depth dependence between (short- and medium-period) seismic noise and seismic waves allows one to improve the signal-to-noise-ratio through appropriate data collection, processing or sensor installation at reasonable depth below the surface (see 4.4).

4.3.3 Long-period seismic noise

At long periods, horizontal noise power may be significantly larger than vertical noise power. The ratio increases with the period and may reach a factor of up to 300 (about 50 dB). A site can be considered as still favorable when the horizontal noise at 100 to 300 s is within 20 dB , as in Fig. 4.25. This is mainly due to tilt, which couples gravity into the horizontal components but not into the vertical (see 5.3.3 and Figs. 5.11 and 5.12). Tilt may be caused by traffic, wind or local fluctuations of barometric pressure. Recording the latter together with the seismic signals may allow correction for this long-period noise (e.g., Beauduin et al. 1996). Other reasons for increased long-period noise may be air circulation in the seismometer vault or underneath the sensor cover. Special care in seismometer *installation* and *shielding* is therefore required in order to reduce drifts and long-period environmental noise (see Chapters 5 and 7).
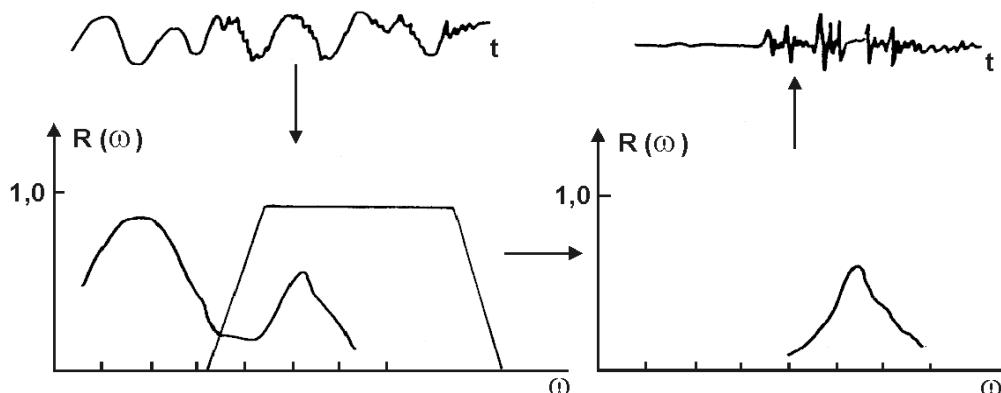
Fig. 4.25 Seismic noise at the station BNG (Bangui, Central Africa) as compared to the new global seismic noise model by Peterson (1963) (from the FDSN Station Book, http://www.fdsn.org/station_book/G/BNG/bng.g_allyr.gif).
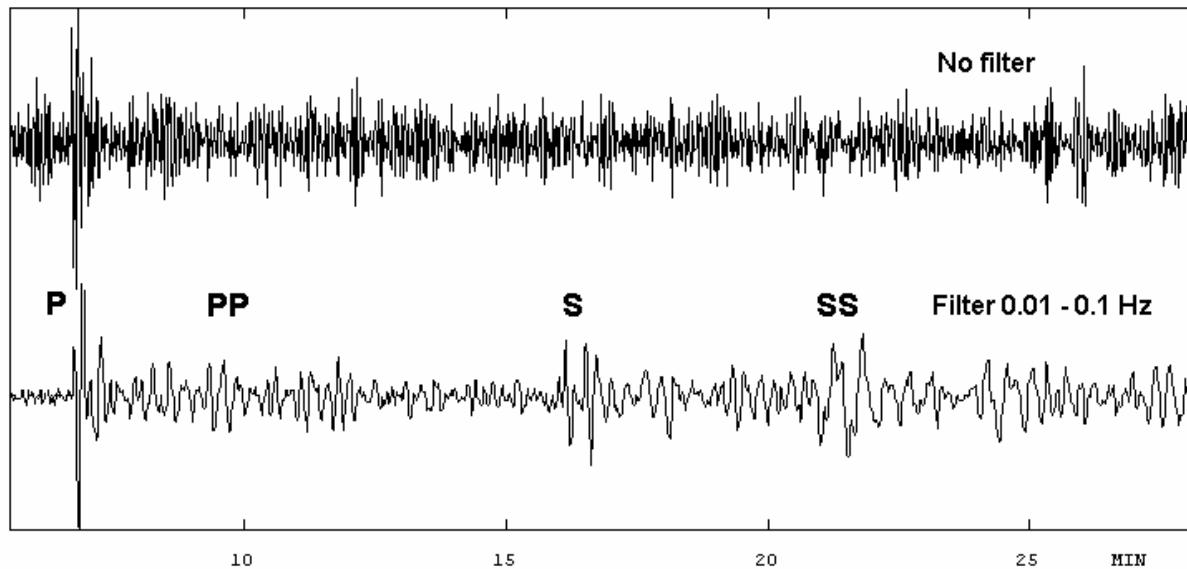
4.4 Measures for improving the signal-to-noise ratio (SNR)

4.4.1 Frequency filtering
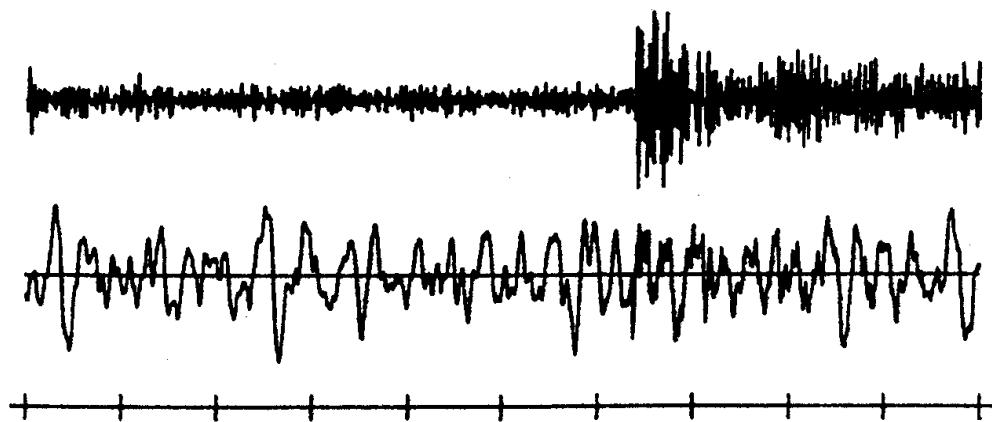
When the frequency spectrum of the seismic signal of interest differs significantly from that of the superposed seismic noise, band-pass filtering can help to improve the signal-to-noise ratio (SNR). Fig. 4.26 illustrates the principle and Figs. 4.27 and 4.28 show examples.

Fig. 4.26 Principle of FOURIER transform and bandpass filtering of a seismic record.

Fig. 4.27 Recording of a LP trace at a broadband station. The LP trace has a flat velocity response from 360 s to 0.5 s. On the unfiltered trace (top), only the P-phase might be identified, while on the filtered trace (bottom), the signal-to-noise ratio is much improved and several later phases are clearly recognizable since the microseisms have been removed by filtering (courtesy of J. Havskov, 2001).
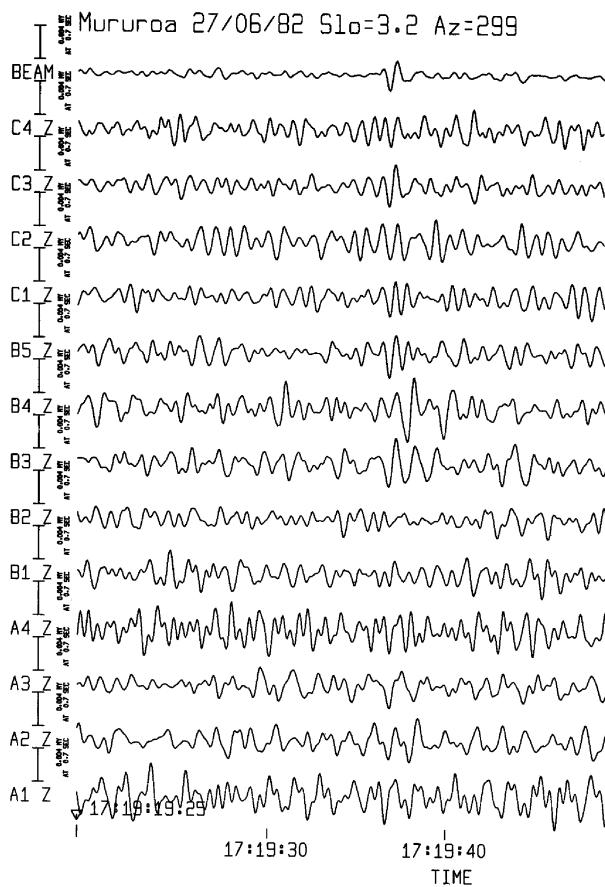

Fig. 4.28 Original (bottom) and frequency filtered record (top; f = 2.0 – 4.0 Hz) of an underground nuclear explosion at the Semipalatinsk test site, Eastern Kazakstan (D = 38°) at station 01A00 of the NORSAR array. Time marks in seconds (from Tronrud, 1983b).

4.4.2 Velocity filtering and beamforming

Often the dominant signal frequencies may coincide with that of strong noise. Then frequency filtering does not improve the SNR. On the other hand, the horizontal propagation velocity of noise (see 4.3.2) is much lower than that of P waves and also lower than that of teleseismic S waves with a steep angle of incidence. This leads to frequency-wavenumber (f-k) filtering (see Chapter 9) as a way to improve SNR. To be able to determine the horizontal propagation direction and velocity of seismic signals by means of signal correlation, a group of seismic

sensors must be deployed. If the aperture (diameter) of the sensor group is within the correlation radius of the signals it is called a seismic array (see Chapter 9); otherwise the group of sensors comprises a station network (see Chapter 8). Assuming that the noise within the array is random while the signal is coherent, even a simple direct summation of the n sensor outputs would already produce some modest SNR improvement. When the direction and velocity of travel of a signal through an array is known, one can compensate for the differences in arrival time at the individual sensors and then sum-up all the n record traces (beam forming). This increases the signal amplitude by a factor n while the random noise amplitudes increase in the beam trace only by √n, thus improving the SNR by √n. Fig. 4.29 compares the (normalized) individual records of 13 stations of the Gräfenberg array, Germany with the beam trace. A weak underground nuclear explosion at a distance of 143.6°, which is not recognizable in any of the single traces, is very evident in the beam trace.


Fig. 4.29 Detection of a weak underground nuclear explosion in the 10 kt range at the Mururoa Atoll test site (D = 145°) by beam forming (top trace). No signal is recognizable in any of the 13 individual record traces from stations of the Gräfenberg array, Germany (below) (from Buttkus, 1986).
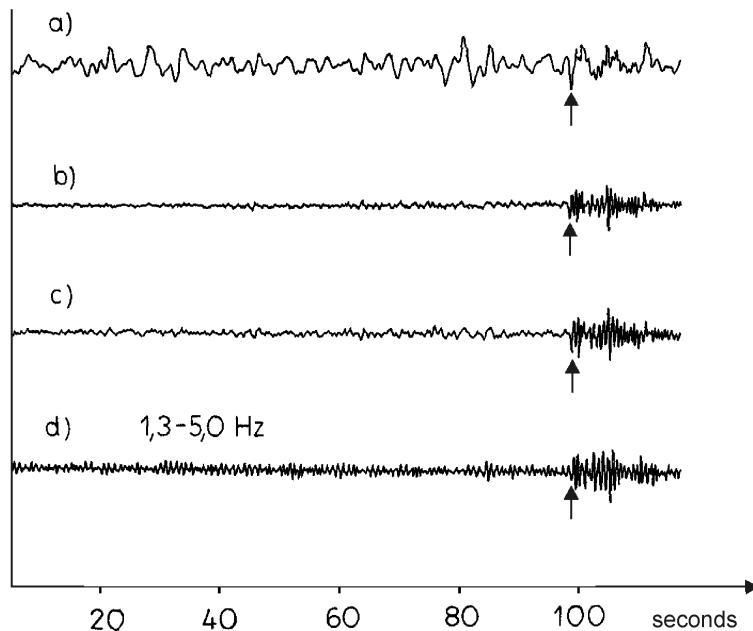
4.4.3 Noise prediction-error filtering

In near real time, it is possible to use a moving time-window to determine the characteristics of a given noise field by means of cross- and auto-correlation of array sensor outputs. This then allows the prediction of the expected random noise in a subsequent time interval. Subtracting the predicted noise time series from the actual record results in a much reduced

noise level. Weak seismic signals, originally buried in the noise but not predicted by the noise "forecast" of the prediction-error filter (NPEF) may then stand out clearly. NPEFs have several advantages as compared to frequency filtering (compare with Fig. 4.30):

- no assumptions on the frequency spectrum of noise are required since actual noise properties are determined by the correlation of array sensor outputs;
- while frequency differences between signal and noise are lost in narrowband filtering, they are largely preserved in the case of the NPEF. This may aid signal identification and onset-time picking;
- signal first-motion polarity is preserved in the NPEF whereas it is no longer certain after zero-phase band-pass filtering (see section 4.2).


Fig. 4.30 Records of an underground nuclear explosion recorded at the Uinta Basin small aperture seismic array a) in the beam trace (sum of 10 seismometers), b) and c) after noise prediction error filtering with and without cross correlation (see 4.4.2) and d) after frequency band-pass filtering (1.3 – 5 Hz) (compiled by Bormann, 1966, from data published by Claerbout, 1964).
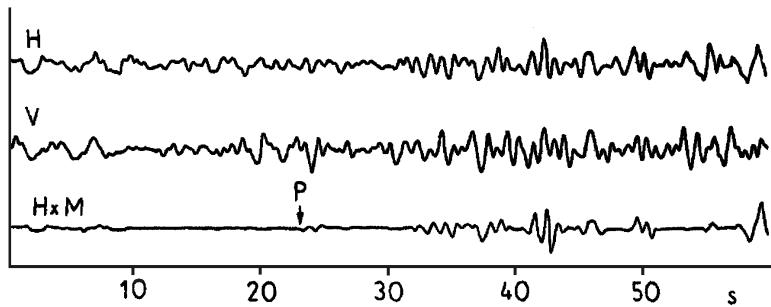
4.4.4 Noise polarization filtering

3-component recordings allow one to reconstruct the ground particle motion and to determine its polarization. Shimshoni and Smith (1964) investigated the cross product

$$M_j = \sum_{i=-n}^{+n} H_{i+j} \cdot V_{i+j} \qquad (4.18)$$

in the time interval $j - n$ to $j + n$ with H and V as the horizontal and vertical component recordings, respectively. M is a measure of the total signal strength as well as of the degree of linear wave polarization. Eq. (4.18) vanishes for Rayleigh, Love and SH waves. On the other

hand, for linearly polarized P and SV waves, *H* and *V* are exactly in phase and the correlation function becomes +1 for P and –1 for SV waves. The longer the integration time, the better the suppression of randomly polarized noise (with a high LR component!). The optimal window length for good noise suppression, while still allowing good onset time picking, must be found by trial and error. Fig. 4.31 gives an example. One great advantage of polarization filtering is that it is independent of differences in the frequency and velocity spectrum of signal and noise and thus can be applied in concert with other procedures for SNR improvement.
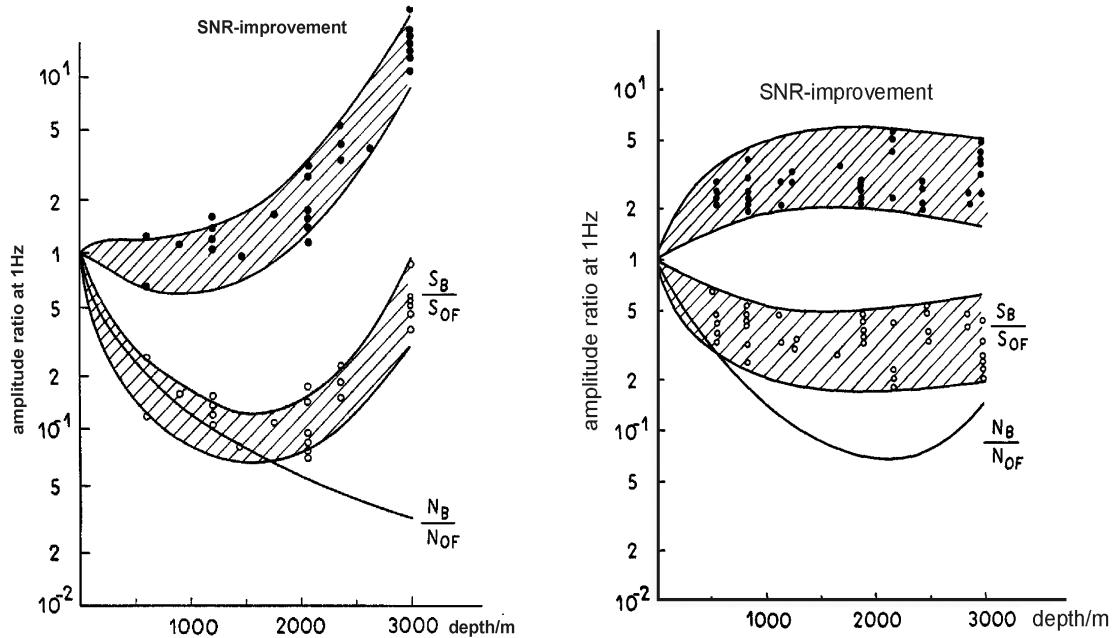

Fig. 4.31 Example of SNR improvement by polarization filtering according to Eq. (4.18) (bottom trace). H – horizontal component record, V – vertical component record (modified from Shimshoni and Smith, 1964).

4.4.5 SNR improvement by recordings in subsurface mines and boreholes
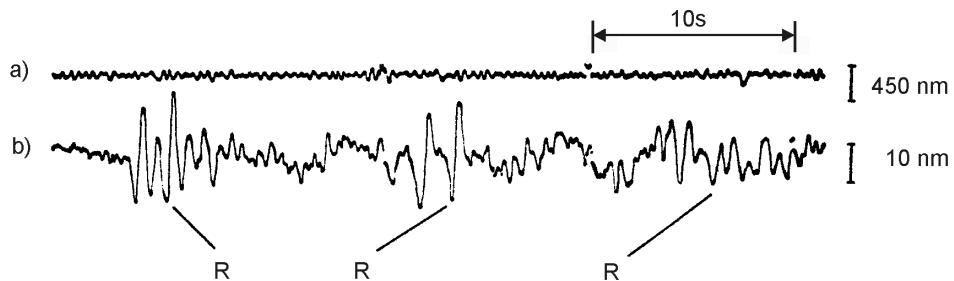
As shown in Figs. 4.23 and 4.24, short-period seismic noise is strongly reduced with the depth of sensor installation in boreholes or mines. However, when installing seismometers at depth, one must also consider effects on the signal. Generally, amplitudes of seismic body waves recorded at the free surface are systematically increased by as much as a factor of two, depending on the incidence angle and wavelength (see Exercise 3.4, Tab. 1). On the other hand, at a certain depth, destructive interference between incoming and surface-reflected waves may cause signal reduction. Therefore, because of the "free-surface effect", peculiarities of the local noise field and geological conditions, the SNR does not necessarily increase steadily with depth. Fig. 4.32 compares two case studies of short-period signal and noise measurements in two deep borehole in the USA.

While in a borehole in Texas the noise amplitudes decreased steadily (up to a factor of 30) down to 3000 m depth below surface, they decreased in another borehole in Oklahoma down to about 2000 m only and then increased again towards larger depth. At this greater depth a layer with 22% lower P-wave velocity was found by means of borehole seismic measurements (traveling noise in a low-velocity layer?). Also, the ratio of the noise in the borehole and at the surface, S_B/S_{OF}, differs in the two boreholes. Its mean value drops in the Texas borehole to 1/10th at about 1500 m depth and increases again to ½ of its surface value at 3000 m depth, while in the Oklahoma borehole it drops to about 1/3 at about 1000 m depth and then remains roughly constant. Accordingly, we have no SNR improvement (on average) in the Texas borehole down to about 1000 m depth, but then the SNR increases to a factor of about 15 at 3000 m depth. Contrary to this, the SNR increases by a factor of 3 in the Oklahoma borehole within the first 800 m, but then remains roughly constant (ranging between 1 and 5) up to 3000 m depth.

Fig. 4.32 Depth dependence of the signal-to-noise ratio (SNR). The top curve in both figures shows the improvement in SNR. The abbreviations are: S_B/S_{OF}: Ratio of signal in borehole and at the surface; N_B/N_{OF}: Ratio of noise in borehole and at the surface. SNR improvement in a borehole in Texas is shown left and in Oklahoma right (redrawn from Douze, 1964).

Therefore it follows that there is no straight-forward and continuous SNR improvement with depth. It may depend also on local geological and installation conditions. Nevertheless, we can generally expect a significant SNR improvement within the first few hundred meters depth. This applies particularly to borehole installations of long-period and broadband sensors which benefit greatly from the very stable temperature conditions and reduced tilt noise at depth. A depth of 100 m is generally sufficient to achieve most of the practicable reduction of long-period noise (-20 to -30 dB) (see 7.4.5). It should also be noted, that in records of deep borehole installation, the superposition of the first arriving waves with their respective surface reflection may cause irritating signal distortions although they can be filtered out by tuned signal processing (Fig. 4.33).
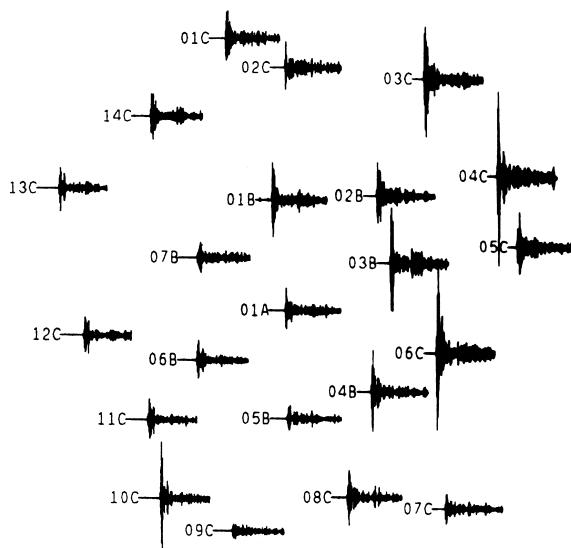

Fig. 4.33 Recording of a teleseismic event at D = 80° at a) the surface and b) at 3000 m depth in the Texas borehole (see Fig. 4.32 left). The SNR improved by a factor of about 10. Note that signal arrivals in the borehole record are followed by related arrivals of the surface reflections (R) about 3 s later (redrawn from Douze, 1964).

For installation depths less than 200 m the travel-time difference between direct and reflected waves is (in consolidated rock) less than 0.1 s and negligible. Since the cost of drilling and installation increases greatly with depth, no deeper permanent seismic borehole installations have yet been made. In any event, the borehole should be drilled through the soil or weathered rock cover and penetrate well into the compacted underlying rock formations.

4.4.6 Signal variations due to local site conditions
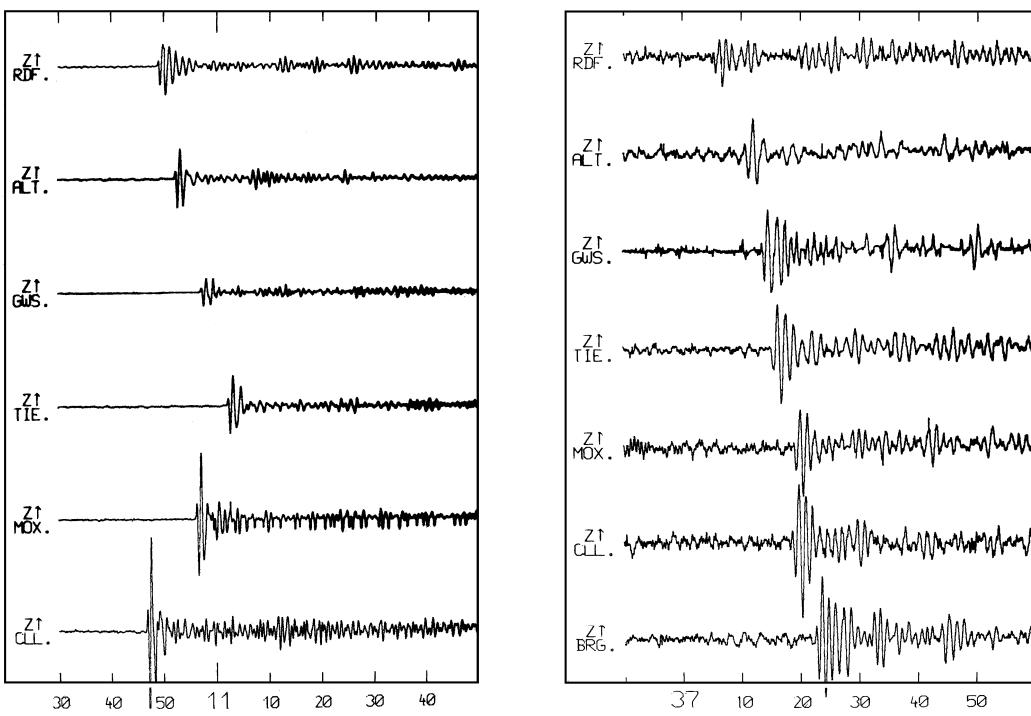
Compared to hard rock sites, both noise and signals may be amplified on soft soil cover. This signal amplification may partly or even fully outweigh the higher noise observed on such sites. Signal strength observed for a given event may vary strongly (up to a factor of about 10 to 30) within a given array or station network, even if its aperture is much smaller than the epicentral distance to the event (< 10-20%), so that differences in backazimuth and amplitude-distance relationship are negligible (Fig. 4.34). Also, while one station of a network may record events rather weakly from a certain source area, the station may do as well as other stations (or even better) for events from another region, azimuth or distance (e.g., station GWS in Fig. 4.35 left and right, respectively).
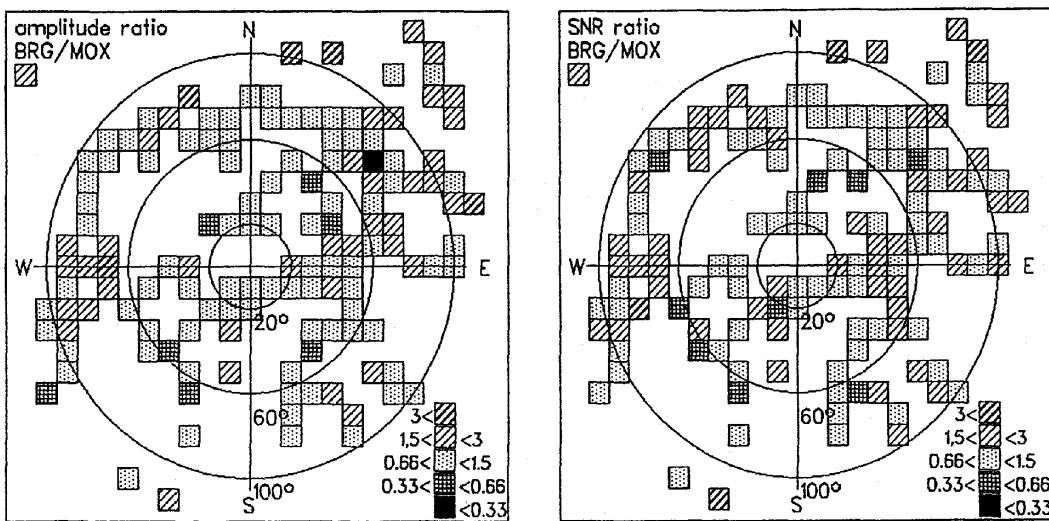

Fig. 4.34 Records of a Semipalatinsk event at stations of the NORSAR seismic array (diameter about 90 km). The event is about 37-38° away. Note the remarkable variations of signal amplitudes by a factor up to 10 (the standard deviation is about a factor of 2) (from Tronrud, 1983a).

Fig. 4.36 compares for regional and teleseismic events the short-period P-wave amplitude ratio (left) and SNR (right) of two stations of the German seismic network. In the same azimuth range, but at different epicentral distances, BRG may record both > 3 times larger as well as > 3 times smaller amplitudes than station MOX. This corresponds to magnitude differences up to one unit! The SNR ratio BGR/MOX also varies by a factor of 3 and more depending on azimuth and distance of events. Therefore, optimal site selection can not be made only on the basis of noise measurements. Also, the signal conditions at possible alternative sites should be compared. These differences in local signal conditions may become negligible in long-period recordings and thus play a lesser role in site selection for broadband networks and arrays.

31

Fig. 4.35 Short-period records of underground nuclear explosions at the test sites of Semipalatinsk (left, D about $41° \pm 1°$) and Nevada (right; D about $81° \pm 1°$) at stations of the former East German seismic network. Note the differences in signal amplitudes both amongst the stations for a given event and for the same station pairs, when comparing events in different azimuth and distance. Also, at right, the compressive first motion is lost in the presence of noise due to the narrowband one-octave recording (see section 4.2.1). Small numbers on the x-axis are seconds, while big numbers are minutes.


Fig. 4.36 Pattern of the relative short-period P-wave amplitudes at station BRG normalized to those of station MOX (170 km apart) in a distance-azimuth polar diagram (reproduced from Physics of the Earth and Planetary Interiors, 69; Bormann et al., "Potsdam seismological station network: …", p. 317, Fig. 7, © 1992; with permission of Elsevier Science).

Acknowledgments

Recommended overview readings (see References under Miscellaneous in Volume 2)

Havskov and Alguacil (2002)
Scherbaum (2001)
Tabulevich (1992)
Webb (2002)

4. Seismic Signals and Noise